Acta Geotechnica
https://doi.org/10.1007/s11440-025-02877-4

RESEARCH PAPER

A novel adhesion–friction-based interface model and its application in generalized load-transfer theoretical analysis for tension–compression composite anchor

Shimin Zhu[1] · Zhuangwei Zhang[1] · Changfu Chen[2] · Genbao Zhang[3] · Mingbin Wang[1]

Received: 23 December 2024 / Accepted: 26 October 2025

Abstract

A recently developed anchorage technique, known as tension–compression composite anchor (TCCA), has gained significant attention from geotechnical engineers. In comparison with tension anchors and compression anchors, TCCA offers superior bearing performance and relatively convenient construction process. This study aims to investigate the load-transfer behaviors of TCCA through theoretical modeling. As a starting step, a novel adhesion–friction-based composite exponential (AFCE) interface model was developed to describe the soil–anchor interface nonlinear mechanical behavior. The parameters of the AFCE interface model can be identified through the utilization of interface shear characteristic values. Despite comprising only three parameters, this model effectively characterizes both the interface softening and hardening behaviors while also accounting for the influence of normal stress. The excellent match between the predicted and measured interface shear stress–displacement curves examined the effectiveness of the AFCE interface model. A generalized load-transfer theoretical framework for TCCA was proposed by integrating the AFCE interface model. Finite element models were established for tension anchor, compression anchor, and TCCA. A detailed analysis was conducted on the bearing capacities and stress distributions for all three types of anchors. The predicted pullout responses agree well with the results from FE simulations as well as from in–situ and laboratory model tests for each type of anchor, proving the extensive applicability of this theoretical framework. Parametric studies were finally conducted to investigate the effect of some key parameters on the bearing capacity of TCCA.

Keywords Interface shear model · Load-transfer analysis · Stress distribution · Tension–compression composite anchor · Theoretical modeling

✉ Shimin Zhu
smzhu@ldu.edu.cn

Zhuangwei Zhang
ZZW13215554663@163.com

Changfu Chen
cfchen@hnu.edu.cn

Genbao Zhang
genbao@hncu.edu.cn

Mingbin Wang
wangmingbin@ldu.edu.cn

[1] School of Hydraulic and Civil Engineering, Ludong University, Yantai 264025, Shandong, China

[2] College of Civil Engineering, Hunan University, Changsha 410082, Hunan, China

[3] College of Civil Engineering, Hunan City University, Yiyang 413000, Hunan, China

Published online: 12 December 2025

1 Introduction

Ground anchor is a kind of geotechnical reinforcement technology that provides many merits, including ease of construction, cost-effectiveness, high bearing capacity, etc. The primary purpose of ground anchor construction is to transfer the external pullout loads to the surrounding stable geomaterial mass through soil/rock–anchor interface resistance, thereby maintaining the structure's stability [4, 17]. This technique was initially developed for mining engineering [8] and has since been extended to deep excavations [19], slopes [7, 28], tunnels [36], and anti-floating buildings [15]. Tension anchors represent the earliest form of anchorage technology used in engineering. However, there are some intrinsic deficiencies for traditional tension anchors, including uneven stress distribution over anchorage segment, load concentration at the anchor head, inadequate mobilization of interface shear strength, and potential tensile cracking of the grout body [45]. These defects can lead to a deterioration in bearing performance for tension anchors during their service period.

In recent decades, the increasing demands of engineering construction have driven continuous innovation in anchorage techniques, leading to the development of various new anchoring structures. Compression anchors were invented to address the defects of tension anchors [1, 12, 16]. A notable characteristic of compression anchors is the separation of cement grout from the internal steel strand or rebar. The grout body of compression anchors is subjected to compressive stress, thus eliminating the risk of tensile cracking. Subsequently, recoverable anchors were developed by upgrading the mechanical connection between reinforcement and bearing plate, allowing for the recycling of steel strand or rebar [21, 37]. However, the aforementioned issues of uneven stress distribution, load concentration, and inadequate mobilization of interface shear strength remain pertinent for compression anchors. The recent development and application of load-distributive compression anchors (LDCA) provided a solution to these problems. Furthermore, the bearing performance of anchoring structure can also be enhanced through the utilization of LDCA [26, 44]. However, the construction of LDCA presents significant challenges and uncertainties because multiple steel strands or rebars must be stretched to specific loads simultaneously using different hydraulic jacks.

A new anchorage technology, namely tension–compression composite anchor (TCCA), has recently gained significant attention from geotechnical engineers [13, 32, 35]. As illustrated in Fig. 1, TCCA consists of both bonded and unbonded segments, with a bearing plate positioned at their junction. The unbonded segment is located in front of the bearing plate, wherein the reinforcement (i.e., steel strand or rebar) is separated from the cement grout through a casing tube. However, the reinforcement and cement grout are affixed together in the bonded segment. The pullout load subjected to the bearing plate via the unbonded steel strand or rebar will be dispersed into two components, including compressive and tensile forces that are exerted on the unbonded and bonded segments, respectively. This design helps alleviate the issues of load concentration and uneven stress distribution associated with tension and compression anchors, so TCCA is equipped with greater bearing capacity. Furthermore, the construction process of TCCA is also relatively convenient.

The bearing performance of ground anchors depends largely on the soil–anchor interface mechanical behaviors [6, 44]. An appropriate interface mechanical model to characterize the soil–anchor interface shear stress–displacement response is of significant importance to the bearing performance assessment for ground anchors. The interface mechanical models can generally be classified into two categories based on their shapes, including broken-line set and curved-line set [4]. Broken-line models are characterized by the shape of a combination of multiple straight lines. Common examples of broken-line interface models include bi-linear hardening model [2], bi-linear softening model [10], tri-linear model [14, 20], four-linear model [27], etc. Typical curved-line interface models include hyperbolic model [34], exponential model [18], rational model [41], etc. Despite the existence of numerous interface mechanical models, these models are usually equipped with some defects, such as an excessive number of parameters and great challenges in determining those parameters. In many cases, the calibration of interface model parameters necessitates the implementation of regression analysis with respect to the measured interface shear stress–displacement curves, particularly with curved-line models. Chen et al. [4] proposed an exponential and rational composite interface model, the four parameters of which can be derived from the utilization of interface mechanical characteristic values and iterative calculation. For compression anchors and TCCAs, the soil–anchor interface normal stress will increase as a consequence of the compression exerted by the grout body on the surrounding soil [31]. However, there is still a lack of interface mechanical models that are capable of considering the effect of normal stress and are equipped with few parameters.

Ground anchors are typically designed with a large ratio of anchorage length to diameter, which inevitably results in the load-transfer problem during the service period [5]. Hence, developing an effective load-transfer model is crucial for assessing the bearing performance of ground

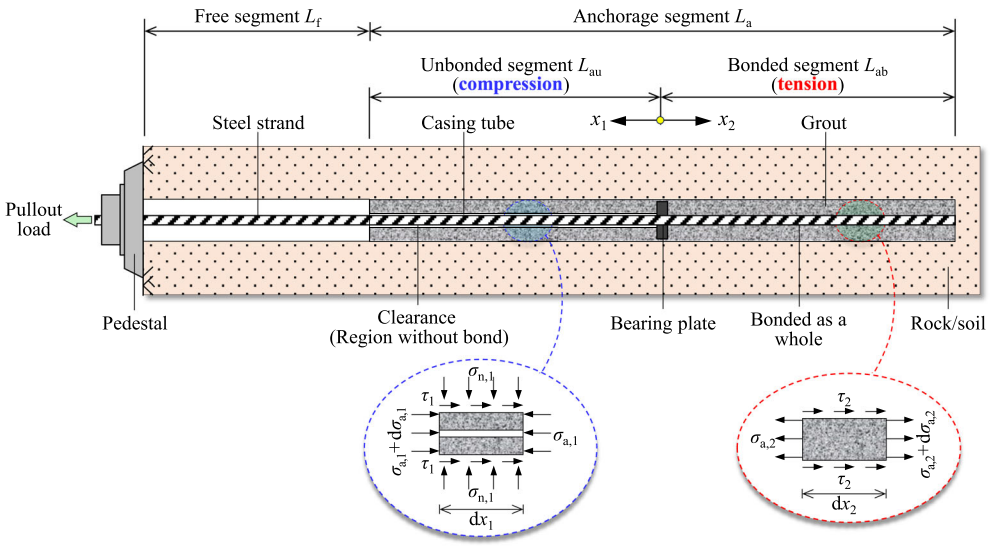

Fig. 1 Component connection and mechanical characteristics of TCCA

anchors. In cases where a broken-line model is utilized to characterize the soil–anchor interface mechanical behaviors, the load-transfer theoretical analysis should be conducted in multiple stages, as it requires piecewise input of interface shear stress [10, 23]. This modeling process is intricate and not convenient for engineers. Obtaining an analytical solution for the load-transfer governing equation becomes difficult when employing a curved-line model to describe the soil–anchor interface mechanical behavior. In spite of this, numerical methods such as the recursion method or finite difference method can be utilized to find solutions that are more accessible for engineers [43]. Overall, the existing load-transfer modeling frameworks mainly focus on tension anchors and compression anchors. Relevant studies about the load-transfer behaviors of TCCA are still scarce, particularly theoretical analyses. Kim et al. [13] investigated the pullout responses of TCCAs through three-dimensional finite element simulations. Tu et al. [30, 33] carried out the in-situ pullout test and the laboratory model test on TCCAs with different proportions of unbonded lengths. A review of the literature indicates that the existing theoretical methods can almost only analyze the bearing performance of a single type of ground anchor. However, there is still a lack of generalized theoretical models capable of analyzing the load-transfer behaviors of tension anchors, compression anchors, and TCCAs simultaneously.

This paper presents a novel adhesion–friction-based composite exponential (AFCE) interface model. This model is equipped with only three parameters, yet capable of characterizing both the interface softening and hardening behaviors while also accounting for the influence of normal stress. Besides, all model parameters can easily be identified through the use of several interface shear characteristic values. These merits are not present in the prevailing interface models, even for those with numerous parameters. A generalized load-transfer theoretical framework for TCCA was then developed, in which the soil–anchor interface mechanical behaviors were characterized by the AFCE interface model. This theoretical framework considered the more complex bearing mechanism of TCCA, particularly the Poisson effect that exists in the unbonded segment. Furthermore, it also has extensive applicability to both traditional tension and compression anchors simultaneously. The theoretically predicted pullout responses of tension anchor, compression anchor, and TCCA were compared with the results obtained from finite element simulations, as well as in-situ and laboratory model experiments. The pullout load–displacement responses and stress distributions of the three types of anchors were also discussed. Finally, parametric studies were conducted to investigate the effect of the proportion of unbonded length, anchorage length, and residual strength ratio on the bearing capacity of TCCAs.

2 Structural and mechanical characteristics of TCCA

The anchorage segment of TCCA consists of two parts: the bonded segment and the unbonded segment, as illustrated in Fig. 1. The unbonded segment is situated in an anterior position, wherein the rebar or steel strand is encased in a casing tube to isolate it from the cement grout. The rebar or steel strand can exhibit tensile deformation without restriction, resulting in the grout being subjected to three-

dimensional compressive stress state. In contrast, the bonded segment is found at the back and lacks a casing tube. The rebar or steel strand and the cement grout are fully glued together and exhibit almost identical deformations. Unlike the unbonded segment, the entire assembly comprising the rebar or steel strand and the grout in the bonded segment exists in axial tensile state. A bearing plate is arranged at the junction of the two sections to exert uniform compressive force on the grout in unbonded segment. The pullout load subjected to the anchor head will be dispersed into two components after being transferred to the bearing plate. This includes the compressive and tensile forces applied to the unbonded and bonded segments, respectively. Hereinto, the compressive force applied to the unbonded segment is derived from the compression exerted by the bearing plate on the grout, and the tensile force applied to the bonded segment should mainly originate from the tension of the steel strand situated behind the bearing plate. The pullout load will finally be conveyed to the surrounding stable soil through the shear or bonding effect of anchoring interface.

The grout body is totally in tensile stress state for traditional tension anchors. There is a decrease in axial force from the head to the end of the whole anchorage segment, with the interface shear strength or interface resistance being mobilized gradually along the axial direction, as shown in Fig. 2a. For compression anchors, the grout body is totally in compressive stress state. The axial force decreases from the end to the head of the anchorage segment, as shown in Fig. 2b. The soil–grout interface normal stress will increase as a consequence of the compression exerted by the grout body on the surrounding soil, which further leads to the increase in interface shear strength. Hence, the bearing capacity of compression anchor is generally larger than that of tension anchor. However, both types of anchors exhibit stress concentration at the loading end, coupled with an inherent limitation in load-transfer along a single direction. Furthermore, the distribution of interface shear stress is markedly uneven over anchorage segment, thereby impeding the synchronous mobilization of interface shear strength, particularly for anchors with long anchorage lengths. In the case of TCCA, the pullout load imposed on the bearing plate is borne by both bonded and unbonded segments. The axial stress of grout body is transferred to both the head and end of the anchorage segment, which is along two directions (Fig. 2c). In comparison with tension and compression anchors, TCCAs can mitigate the issue of stress concentration to a certain extent and can also facilitate the simultaneous operation of interface shear strength over both bonded and unbonded segments. It is undoubtedly beneficial to improve the bearing capacity of the anchoring structure.

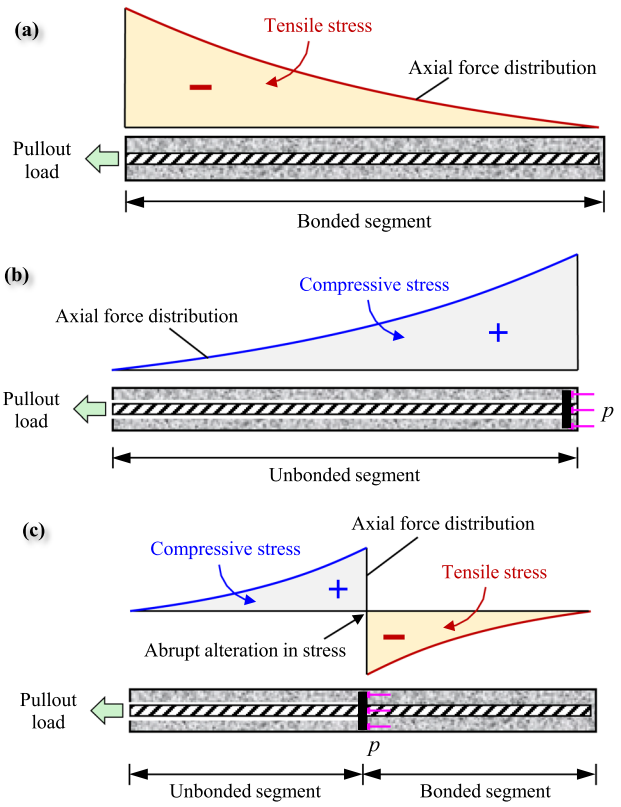

Fig. 2 Axial force distributions of three types of anchors: **a** Tension anchor; **b** Compression anchor; **c** TCCA

3 A novel adhesion–friction-based composite exponential interface model

3.1 Model establishment

The interface shear strength between soil and anchor grout can generally be divided into two main components: interface adhesion and interface friction [4, 22], as shown in Fig. 3. The mobilization of soil–anchor interface shear strength parallels the behavior observed in soil shear strength [9]. Interface adhesion τ_c may arise from a combination of electrostatic attraction, van der Waals forces, and interparticle chemical cohesion. Interface adhesion τ_c increases with increasing interface shear displacement s. Once the interface shear displacement s exceeds a specific threshold that is denoted as $s_{c,f}$, interface adhesion τ_c will gradually decrease to zero due to the debonding of the anchoring interface. Interface friction τ_s primarily develops from slip displacement over the soil–anchor interface. It is influenced by normal stress, interface roughness, etc. Interface friction is expected to increase with interface shear displacement s until it tends to a specific value $\tau_{s,f}$.

Double and single exponential functions were employed to describe the relationship between interface adhesion τ_c

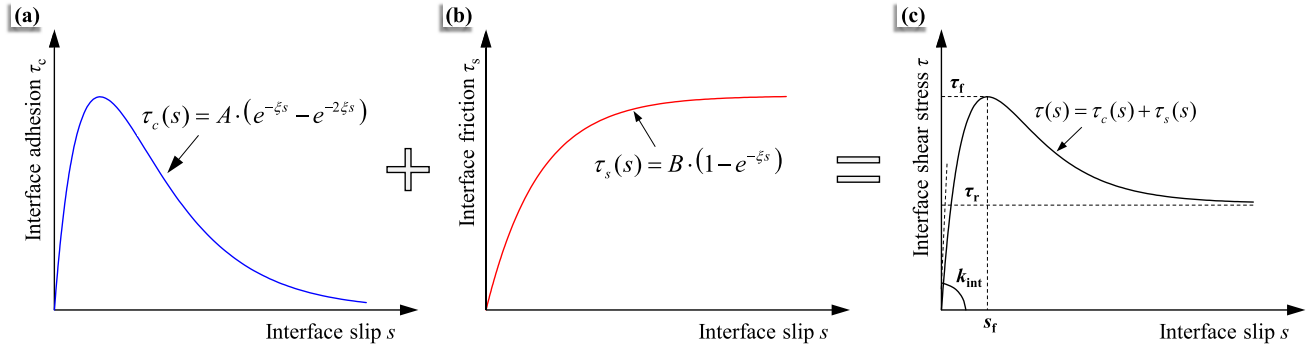

Fig. 3 Mobilization mechanism of soil–anchor interface shear strength: **a** Evolution of interface adhesion; **b** Evolution of interface friction; **c** The observed interface mechanical response

and interface friction τ_s with displacement s, respectively. It can be expressed by Eq. (1).

$$\begin{cases} \tau_c(s) = A \cdot \left(e^{-\xi s} - e^{-2\xi s}\right) \\ \tau_s(s) = B \cdot \left(1 - e^{-\xi s}\right) \end{cases} \tag{1}$$

where A, B, and ξ are three model parameters. Among those, parameters A and B control the peak values of interface adhesion τ_c and interface friction τ_s, respectively. The parameter ξ controls the interface peak shear displacement s_f and the shape of the τ-s curve.

The adhesion–friction-based composite exponential (AFCE) interface model can be established through a combination of interface adhesion τ_c and interface friction τ_s, which is expressed as follows:

$$\tau(s) = \tau_c(s) + \tau_s(s) = A \cdot \left(e^{-\xi s} - e^{-2\xi s}\right) + B \cdot \left(1 - e^{-\xi s}\right) \tag{2}$$

where $\tau(s)$ is the observed interface shear stress.

3.2 Model parameters determination

The aforementioned three model parameters, designated A, B, and ξ, can be identified through regression analysis applied to the measured τ-s curve. Noteworthy that the testing for τ-s curve is relatively convenient in laboratory but considerably challenging in field. In the absence of τ-s curve, the three model parameters can also be determined by utilizing some interface mechanical characteristic values. These include peak interface shear strength τ_f, residual strength ratio η, peak shear displacement s_f, and initial interfacial shear stiffness k_{int}. η is defined as the ratio of residual interface shear strength τ_r to peak interface shear strength τ_f.

$$\eta = \tau_r / \tau_f \tag{3}$$

Three interface mechanical characteristic values are sufficient to determine the model parameters of A, B, and ξ. Among the four characteristic values, obtaining k_{int} poses the greatest difficulty and uncertainty. Hence, τ_f, η, and s_f were specially selected to ascertain the interface model parameters. Further details are explained below.

Condition 1: peak shear displacement s_f corresponds to peak interface shear strength τ_f.

$$\tau(s_f) = A \cdot \left(e^{-\xi s_f} - e^{-2\xi s_f}\right) + B \cdot \left(1 - e^{-\xi s_f}\right) = \tau_f \tag{4}$$

Condition 2: the derivative of the interface model (Eq. 2) is equal to zero at the point $s = s_f$.

$$\left.\frac{d\tau(s)}{ds}\right|_{s=s_f} = A \cdot \left(2\xi e^{-2\xi s_f} - \xi e^{-\xi s_f}\right) + \xi B e^{-\xi s_f} = 0 \tag{5}$$

Condition 3: interface shear stress τ tends to residual strength τ_r when shear displacement s develops infinitely.

$$\begin{aligned} \lim_{s\to\infty} \tau(s) &= \lim_{s\to\infty} A \cdot \left(e^{-\xi s} - e^{-2\xi s}\right) + B \cdot \left(1 - e^{-\xi s}\right) = \tau_r \\ &= \eta \cdot \tau_f \end{aligned} \tag{6}$$

Combining Eqs. (4–6), the model parameters of A, B, and ξ were derived as:

$$\begin{cases} A = (2 - \eta + 2\sqrt{1-\eta}) \cdot \tau_f \\ B = \eta \cdot \tau_f \\ \xi = \ln\left(\dfrac{2 - \eta + 2\sqrt{1-\eta}}{1 - \eta + \sqrt{1-\eta}}\right) \cdot \dfrac{1}{s_f} \end{cases} \tag{7}$$

By substituting Eq. (7) into Eq. (2), the interface shear model can be transformed into the following form.

$$\tau(s) = \tau_f \cdot \left[(k_1 - \eta) e^{-k_2 \frac{s}{s_f}} - k_1 e^{-2k_2 \frac{s}{s_f}} + \eta\right] \tag{8}$$

where

$$\begin{cases} k_1 = 2 - \eta + 2\sqrt{1-\eta} \\ k_2 = \ln\left(\dfrac{2 - \eta + 2\sqrt{1-\eta}}{1 - \eta + \sqrt{1-\eta}}\right) \end{cases} \tag{9}$$

Equation (8) can accordingly be used to establish an interface model that characterizes the soil–anchor interface nonlinear mechanical behaviors, provided that the

aforementioned three interface mechanical characteristic values have been obtained. The current form of the AFCE interface model is inadequate in accounting for the soil–grout interface normal stress. Hence, Mohr–Coulomb's law [6] was specially incorporated to facilitate improvement. The relationship between peak shear strength τ_f and interface normal stress σ_n can be expressed as follows:

$$\tau_f = c_\tau + \sigma_n \cdot \tan \varphi_\tau \tag{10}$$

where c_τ represents interface apparent cohesion, which can be regarded as the peak shear strength without applying additional normal stress; and φ_τ represents interface friction angle.

Residual strength ratio η and peak shear displacement s_f do not generally exhibit changes in response to variations in interface normal stress σ_n. Hence, the interface shear model capable of elucidating the effect of interface normal stress can be established by substituting Eq. (10) into Eq. (8), as expressed in Eq. (11).

$$\tau(s) = (c_\tau + \sigma_\mathrm{n} \cdot \tan \varphi_\tau) \cdot \left[(k_1 - \eta)e^{-k_2 \frac{s}{s_\mathrm{f}}} - k_1 e^{-2k_2 \frac{s}{s_\mathrm{f}}} + \eta\right] \tag{11}$$

Noteworthy that Eq. (11) describes the incomplete interface softening behavior, which is actually the general soil conditions. In practice, there are two special cases.

Special case 1: complete interface softening. That is, residual interface shear strength $\tau_\mathrm{r} \approx 0$ and residual strength ratio $\eta \approx 0$. This situation applies to anchors embedded in very sticky or hard geomaterials, such as those in resin [18] or rocks [25]. The interface model can be rewritten as:

$$\tau(s) = \tau_c(s) = A \cdot \left(e^{-\xi s} - e^{-2\xi s}\right) \tag{12}$$

The two model parameters of A and ξ existing in Eq. (12) can be determined by the utilization of peak shear strength τ_f and peak shear displacement s_f, as expressed in Eq. (13).

$$\begin{cases} A = 4 \cdot \tau_\mathrm{f} \\ \xi = \ln\left(\dfrac{4}{3}\right) \cdot \dfrac{1}{s_\mathrm{f}} \end{cases} \tag{13}$$

Special case 2: interface hardening. That is, residual interface shear strength $\tau_\mathrm{r} \approx \tau_f$ and residual strength ratio $\eta \approx 1$. This case pertains to anchors embedded in cohesionless soil, such as those in loose sand. The interface model can be rewritten as:

$$\tau(s) = \tau_s(s) = B \cdot \left(1 - e^{-\xi s}\right) \tag{14}$$

The two model parameters of B and ξ existing in Eq. (14) can be determined by the utilization of peak shear strength τ_f and initial interface shear stiffness k_int, as expressed in Eq. (15).

$$\begin{cases} B = \tau_\mathrm{f} \\ \xi = \dfrac{k_\mathrm{int}}{\tau_\mathrm{f}} \end{cases} \tag{15}$$

The prevailing interface shear models are generally equipped with numerous parameters, yet it proves challenging to articulate both the interface softening and hardening behaviors. Some interface models, despite processing few parameters, are only compatible with specific working conditions. The proposed AFCE interface shear model comprises only three parameters, yet it is capable of characterizing both the interface softening and hardening behaviors. The effect of interface normal stress can also be considered. The model parameters can be easily determined by using three interface mechanical characteristic values. Additionally, this model enables the prediction of the interface shear stress–displacement response. Overall, the development of the AFCE interface shear model facilitates a simpler analysis procedure concerning the complicated soil–anchor interface mechanical properties. Nevertheless, the proposed model cannot be suitable for all engineering conditions due to the complexity of soil–anchor interface mechanical behaviors. For example, it is assumed that the peak interface shear displacement s_f does not vary with interface normal stress σ_n. Hence, the calculation accuracy of this model will deteriorate if there is a considerable change observed in s_f in response to a variation in σ_n.

3.3 Verification for the AFCE interface model

Element-scale pullout test and direct shear test are the two most frequently used techniques for obtaining the soil–anchor interface shear stress–displacement responses. Hereinto, the element-scale pullout test can simulate the construction process and stress conditions of the anchors, thereby ensuring that the measured soil–anchor interface mechanical behaviors closely match the actual responses. However, it is unfeasible to apply normal stress directly on the soil–anchor interface in element-scale pullout test due to the soil arch effect. In contrast, the direct shear test allows for better control of the soil–anchor interface normal stress. In the following sections, the test data collected from both types of tests would be used to validate the accuracy of the AFCE interface model.

3.3.1 Element-scale pullout tests

The present study employed element-scale pullout test to investigate the interface mechanical behaviors between red clay and grouted anchors. The pullout specimen was cylindrical, with external diameter of 20 cm, anchor hole diameter of 2 cm, and bonded length of 8 cm. The grouting

material was cement paste with water–cement ratio of 0.45. After the grouting material was fully cured, the grout body was pulled out of the red clay at a controlled displacement rate of 1 mm/min by using a specially developed device. Accordingly, the red clay–anchor interface shear stress τ—displacement s curve could be obtained through this method. The properties of all materials and the testing procedures had been expounded extensively in previous works by Chen and Zhu [3]. In this test, no confining pressure was applied to the specimen, resulting in the additional normal stress being equal to zero at the soil–anchor interface.

The measured τ-s curve was analyzed to determine the interface mechanical characteristic values, including τ_f = 126 kPa, s_f = 2.0 mm, and η = 0.28. Subsequently, the three interface model parameters could further be calculated by Eq. (7), yielding A = 430.5 kPa, B = 35.3 kPa, and ξ = 0.39 mm^{-1}. The prediction derived from the AFCE interface model (Eq. 8) was compared with the measured τ-s curve, as illustrated in Fig. 4. The close agreement between the predictions and measurements indicates that the proposed model can accurately predict the soil–anchor interface mechanical behavior. The evolution contribution of adhesion and friction is also exhibited in Fig. 4. It can be observed that as the displacement s increases to 1.90 mm, the interface adhesion is mobilized to the maximum value of 107.4 kPa, after which it gradually decreases to zero. Meanwhile, the interface friction increases with increasing shear displacement. When the shear displacement s exceeds 6.4 mm, the interface friction surpasses interface adhesion, thereby occupying the predominant position and eventually stabilizing at the value of 35.3 kPa.

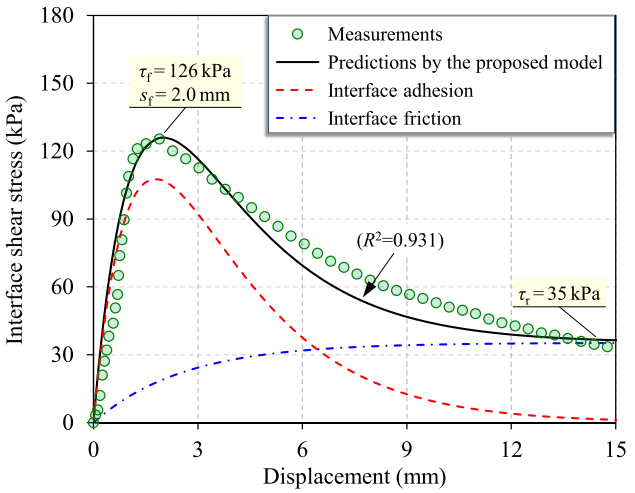

Fig. 4 Comparison of red clay–anchor interface shear curve between the element-scale pullout test results and the model predictions as well as the evolution contribution of interface adhesion and interface friction

Zhang et al. [40] investigated the effect of soil moisture content on the soil–anchor interface mechanical responses through a series of element-scale pullout tests. The measured τ-s curves with soil moisture contents w of 18.1%, 20.2%, and 28.1% were selected for model validation. The additional interface normal stress is equal to zero owing to the absence of confining pressure. The disparate soil moisture content is responsible for the difference in the soil–anchor interface mechanical responses. The test data were analyzed to determine the interface mechanical characteristic values and the three interface model parameters. The results are summarized in Table 1. A comparison of the measured and predicted τ-s curves is presented in Fig. 5. It is evident that the correlation coefficients R^2 between the test results and the model predictions are all higher than 0.93 for the three groups of tests, and the shapes of τ-s curves also exhibit favorable agreement.

3.3.2 Interface direct shear tests

Toufigh et al. [29] conducted direct shear tests for polymer concrete–sand interface under normal stress σ_n of 50 kPa, 120 kPa, and 200 kPa. The test results from the rough surface of ordinary concrete (OCR) were collected to verify the proposed AFCE interface model. Hu and Pu [11] investigated the effect of surface roughness on the sand–structure interface mechanical characteristics through direct shear tests. The test results pertaining to the soil relative density D_r of 90% and interface relative roughness R_n of 0.5 were employed for the interface model verification. The normal stresses applied to the soil–structure interface were 50 kPa, 100 kPa, 200 kPa, and 400 kPa in these tests. Figure 6 depicts the relationship between the peak interface shear strength τ_f and residual interface shear strength τ_r with normal stress σ_n in the two groups of tests. Mohr–coulomb formula (Eq. 10) was adopted to determine the interface apparent cohesion c_τ and interface friction angle φ_τ. Table 2 summarizes the interface model parameters for the two groups of tests. Accordingly, the AFCE

Table 1 Soil–anchor interface characteristic values and AFCE model parameters of the element-scale pullout tests conducted by Zhang et al. [40]

	w = 18.1%	w = 20.2%	w = 28.1%
τ_f (kPa)	70	54	25
s_f (mm)	3.0	3.0	4.2
η	0.60	0.62	0.70
A (kPa)	186.5	141.1	59.9
B (kPa)	42.0	33.5	17.5
ξ (mm^{-1})	0.32	0.32	0.25

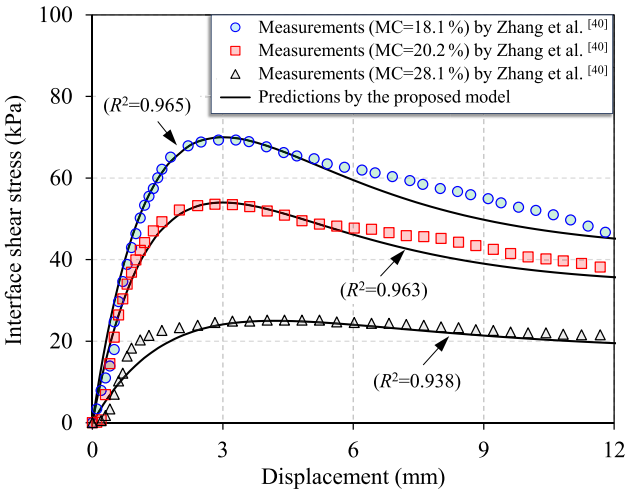

Fig. 5 Comparisons of the measured and predicted soil–anchor interface shear curves (the data were derived from element-scale pullout test conducted by Zhang et al. [40])

interface models with normal stress being considered were derived by substituting these model parameters into Eq. (11).

As shown in Fig. 7, the predicted τ-s curves under different normal stresses all matched well with the measurements. The correlation coefficient R^2 between the test results and the model predictions was consistently above 0.90. These positive outcomes adequately demonstrated the accuracy of the developed AFCE interface model.

Table 2 Model parameters of interface direct tests

Properties	Tests from Toufigh et al. [29]	Tests from Hu and Pu [11]
c_τ (kPa)	0.5	28.7
φ_τ (°)	31.5	40.1
s_f (mm)	2.8	1.4
η	0.70	0.63

4 A generalized theoretical framework for the load-transfer analyses of TCCA

4.1 Basic assumptions

The pullout load was borne by both bonded and unbonded segments for TCCA. In the unbonded segment, the soil–grout interface normal stress increases as a consequence of the compression exerted by the grout body on the surrounding soil. This phenomenon is known as the Poisson effect. Hence, interface normal stress should be considered in the load-transfer theoretical framework for TCCA. Furthermore, the load sharing between bonded segment and unbonded segment presents additional challenges to the theoretical analysis. To simplify the modeling process, the following assumptions were stipulated:

(a) The cement grout, steel strand, and surrounding soil are all elastic, and their mechanical behaviors are in accordance with Hooke's law.

(b) The diameter of steel strand is significantly smaller than that of grout body. Hence, the anchor hole reserved in grout body is ignored, and the grout body

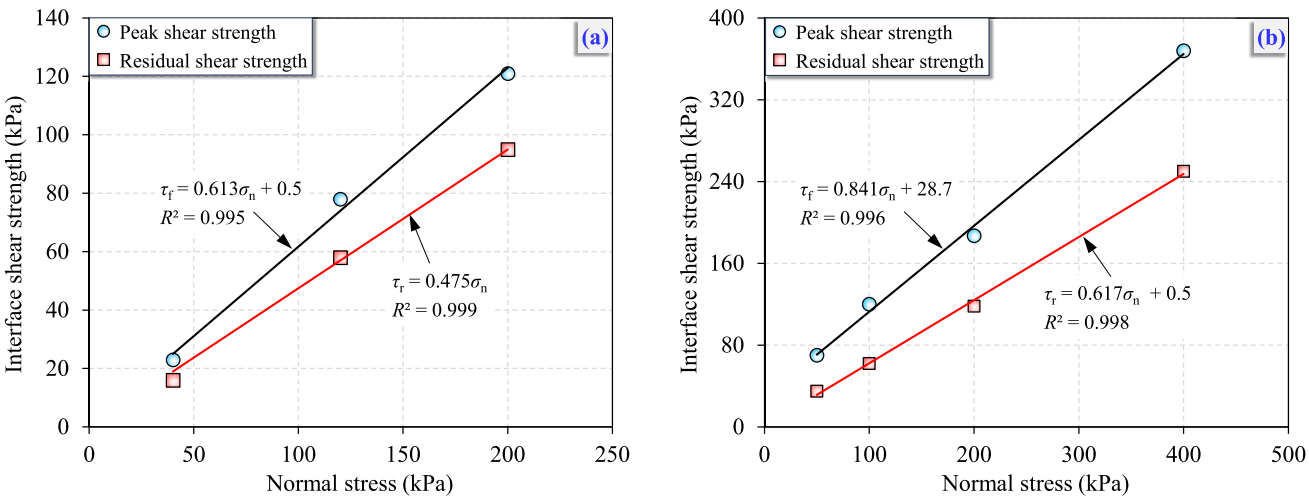

Fig. 6 Mohr–Coulomb failure envelopes of the interface peak shear strength and the interface residual shear strength: **a** Test data from Toufigh et al. [29]; **b** Test data from Hu and Pu [11]

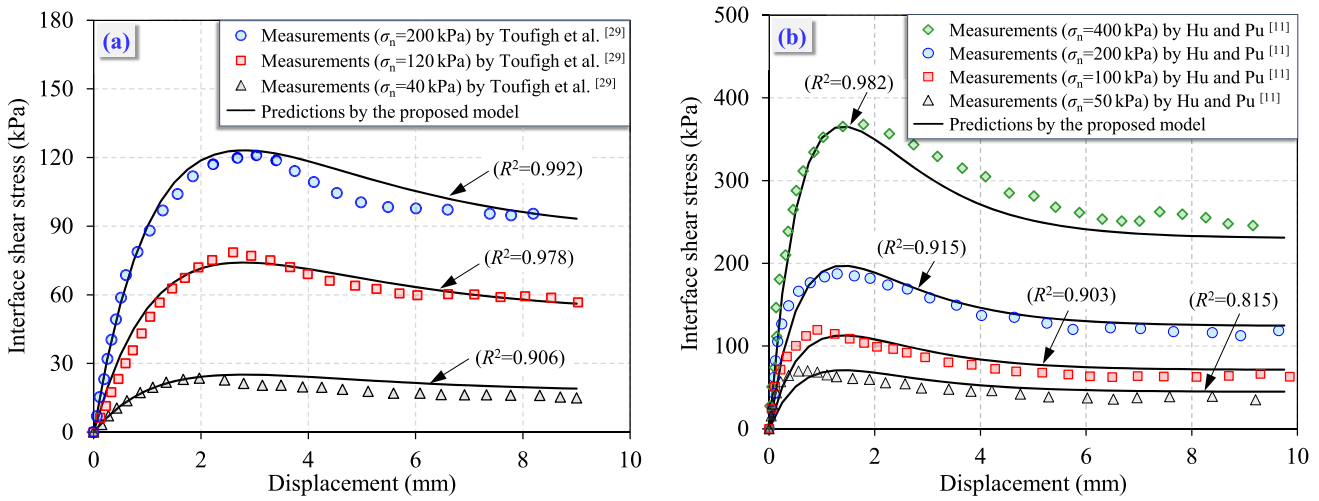

Fig. 7 Comparisons of the soil–anchor interface shear curves between the model predictions and the interface direct shear test results: **a** Test data from Toufigh et al. [29]; **b** Test data from Hu and Pu [11]

in unbonded segment is regarded as a homogeneous cylinder.

(c) Ignoring the difference in diameter between bearing plate and grout body. The pullout load subjected to the bearing plate is uniformly distributed across the entire cross section of the grout body.

(d) The increase in soil–grout interface normal stress caused by Poisson's effect in the unbonded segment is modeled by the combined utilization of cavity expansion theory and the AFCE interface model. However, the interface normal stress is not considered in the bonded segment due to the shrinkage of grout diameter caused by tensile force.

(e) The shear/bond strength observed in the steel strand–grout interface is considerably superior to that of the soil–grout interface. These two interface shear strengths may differ by dozens of times. Grouted anchors, particularly those embedded in soil, generally fail at the soil–grout interface, while the grout and steel strand exhibit strong adhesion, and their deformations are synchronous. Hence, to simplify the modeling process, it is assumed that the steel strand and the grout as a whole demonstrated synchronized deformation within the bonded segment.

4.2 Basic equations of load-transfer theoretical model

Figure 1 depicts the analytical schematic for the load-transfer behavior of TCCA. The TCCA is L in total length, L_a in anchorage length, and L_f in free length. The bonded and unbonded lengths are L_{ab} and L_{au}, respectively. Two local coordinate systems, designated x_1 and x_2, were established with coordinate origin situated at the heads of the bonded and unbonded segments, that is, at the front and the back of the bearing plate. Subsequently, micro-segments of the grout body derived from both bonded and unbonded segments were selected for theoretical analysis.

4.2.1 Unbonded segment

In accordance with assumption (a), the grout body is in elastic state, so its axial strain $\varepsilon_{a1}(x_1)$ in unbonded segment can be represented by Eq. (16).

$$\varepsilon_{a1}(x_1) = \frac{1}{E_g}\left[\sigma_{a1}(x_1) - 2\nu_g\sigma_{n1}(x_1)\right] \tag{16}$$

where E_g and ν_g are Young's modulus and Poisson's ratio of the grout body; and $\sigma_{a1}(x_1)$ and $\sigma_{n1}(x_1)$ are axial stress and interface normal stress in unbonded segment.

According to Hooke's law, the radial expansion strain of grout body $\varepsilon_{r1}(x_1)$ is determined as follows:

$$\varepsilon_{r1}(x_1) = \frac{1}{E_g}\left[\nu_g\sigma_{a1}(x_1) + (\nu_g - 1)\sigma_{n1}(x_1)\right] \tag{17}$$

It was assumed that the soil or rock was in elastic state. Hence, the radial strain of the soil or rock around the grout body $\varepsilon_{sr1}(x_1, r_1)$ can be derived using cavity expansion theory.

$$\varepsilon_{sr1}(x_1, r_1) = \frac{(1+\nu_s)}{E_s}\frac{r_0^2}{r_1^2}\sigma_{n1}(x_1) \tag{18}$$

where E_s and ν_s are Young's modulus and Poisson's ratio of the surrounding soil or rock; r_0 is radius of the grout body; and r_1 is displacement from the center of the anchor hole in unbonded segment.

The radial strain of grout body is equal to that of the soil or rock at the wall of anchor hole ($r = r_0$), which can be expressed as Eq. (19).

$$\varepsilon_{\mathrm{r1}}(x_1) = \varepsilon_{\mathrm{sr1}}(x_1, r_0) \tag{19}$$

The relationship between axial stress $\sigma_{\mathrm{a1}}(x_1)$ and interface normal stress $\sigma_{\mathrm{n1}}(x_1)$ of the grout body can be derived from a synthesis of Eqs. (17) to (19).

$$\sigma_{\mathrm{n1}}(x_1) = \lambda \cdot \sigma_{\mathrm{a1}}(x_1) \tag{20}$$

where $\lambda = \frac{v_g E_s}{E_g(1+v_s)+E_s(1-v_g)}$.

The axial compression deformation of the grout micro-segment can be calculated by subtracting the interface shear displacement at either end. Therefore, the geometric equation describing the relationship between the grout axial strain $\varepsilon_{a1}(x_1)$ and the interface shear displacement $s_1(x_1)$ can further be established:

$$\varepsilon_{\mathrm{a1}}(x_1) = -\frac{ds_1(x_1)}{dx_1} \tag{21}$$

Force equilibrium equation for the grout micro-segment was derived through the analysis of its static force condition, which can be expressed as follows:

$$\frac{d\sigma_{\mathrm{a1}}(x_1)}{dx_1} + \frac{u_{\mathrm{p}}}{A}\tau_1(x_1) = 0 \tag{22}$$

where A and u_p represent the cross-sectional area and perimeter of the anchor hole; and $\tau_1(x_1)$ represents the interface shear stress in unbonded segment.

The load-transfer governing equation for unbonded segment can be deduced by combining Eqs. (16), (20–22).

$$\frac{\mathrm{d}^2 s_1(x_1)}{\mathrm{d}x_1^2} + \frac{\mu_{\mathrm{p}}(2\lambda v_{\mathrm{g}} - 1)}{E_{\mathrm{g}}A}\tau_1(s_1) = 0 \tag{23}$$

The normal stress is exerted at the anchoring interface in unbonded segment. Hence, the developed AFCE interface model with normal stress considered (Eq. 11) was integrated into Eq. (23) to characterize the soil–anchor interface mechanical responses. This equation is then combined with Eqs. (16), (20), and (21) to yield a new form of the load-transfer governing equation.

$$\frac{\mathrm{d}^2 s_1(x_1)}{\mathrm{d}x_1^2} + h_1 f(s_1)\frac{\mathrm{d}s_1(x_1)}{\mathrm{d}x_1} + h_2 f(s_1) = 0 \tag{24}$$

where

$$\begin{cases} h_1 = \dfrac{\lambda\mu_{\mathrm{p}}\tan\varphi_\tau}{A} \\ h_2 = \dfrac{\mu_{\mathrm{p}}c_\tau(2\lambda v_{\mathrm{g}} - 1)}{E_{\mathrm{g}}A} \\ f(s_1) = (k_1 - \eta)e^{-k_2\frac{s_1}{s_{\mathrm{f}}}} - k_1 e^{-2k_2\frac{s_1}{s_{\mathrm{f}}}} + \eta \end{cases} \tag{25}$$

4.2.2 Bonded segment

In accordance with assumption (d), there is no extra interface normal stress in the bonded segment. The steel strand and the grout material remain securely attached, together forming the anchor body. Consequently, the tensile strain of the anchor body $\varepsilon_{\mathrm{a2}}(x_2)$ can be represented as:

$$\varepsilon_{a2}(x_2) = \sigma_{a2}(x_2)/E_{\mathrm{bg}} \tag{26}$$

where E_{bg} is the composite modulus of the anchor body, $E_{bg} = \frac{E_g A_g + E_b A_b}{A}$; E_{g} and E_{b} are the Young's modulus of the grout body and the steel strand; and A_{g} and A_b are the cross-sectional area of the grout body and the steel strand.

The geometric equation describing the relationship between the axial tensile strain $\varepsilon_{\mathrm{a2}}(x_2)$ and the interface shear displacement $s_2(x_2)$ in the bonded segment is expressed as:

$$\varepsilon_{\mathrm{a2}}(x_2) = -\frac{ds_2(x_2)}{dx_2} \tag{27}$$

The force equilibrium equation for the anchor microsegment in bonded segment is derived as:

$$\frac{d\sigma_{\mathrm{a2}}(x_2)}{dx_2} + \frac{u_{\mathrm{p}}}{A}\tau_2(x_2) = 0 \tag{28}$$

By combining Eqs. (26)–(28), the load-transfer governing equation can be derived:

$$\frac{\mathrm{d}^2 s_2(x_2)}{\mathrm{d}x_2^2} - \frac{u_{\mathrm{p}}}{E_{\mathrm{bg}}A}\tau_2(s_2) = 0 \tag{29}$$

By substituting Eq. (11) into Eq. (29) and taking interface normal stress $\sigma_{\mathrm{n}} = 0$, the load-transfer governing equation for the bonded segment can be rewritten as:

$$\frac{\mathrm{d}^2 s_2(x_2)}{\mathrm{d}x_2^2} - \frac{u_{\mathrm{p}}c_\tau}{E_{\mathrm{bg}}A}\cdot\left[(k_1 - \eta)e^{-k_2\frac{s_2}{s_{\mathrm{f}}}} - k_1 e^{-2k_2\frac{s_2}{s_{\mathrm{f}}}} + \eta\right] = 0 \tag{30}$$

4.2.3 Boundary conditions

Boundary condition (1): the axial stresses of the grout body are equal to zero at the ends of the bonded and unbonded segments ($x_1 = L_{\mathrm{au}}$, $x_2 = L_{\mathrm{ab}}$).

$$\begin{cases} \sigma_{a1,L_{\mathrm{au}}} = 0 \\ \sigma_{a2,L_{\mathrm{ab}}} = 0 \end{cases} \tag{31}$$

Boundary condition (2): as illustrated in Fig. 8, the steel strand and the grout are fully separated by a casing tube in unbonded segment. Therefore, the pullout load P applied to the anchor head can be transferred without any loss to the bearing plate through the steel strand in the free and unbonded segments. The pullout load P is then divided into

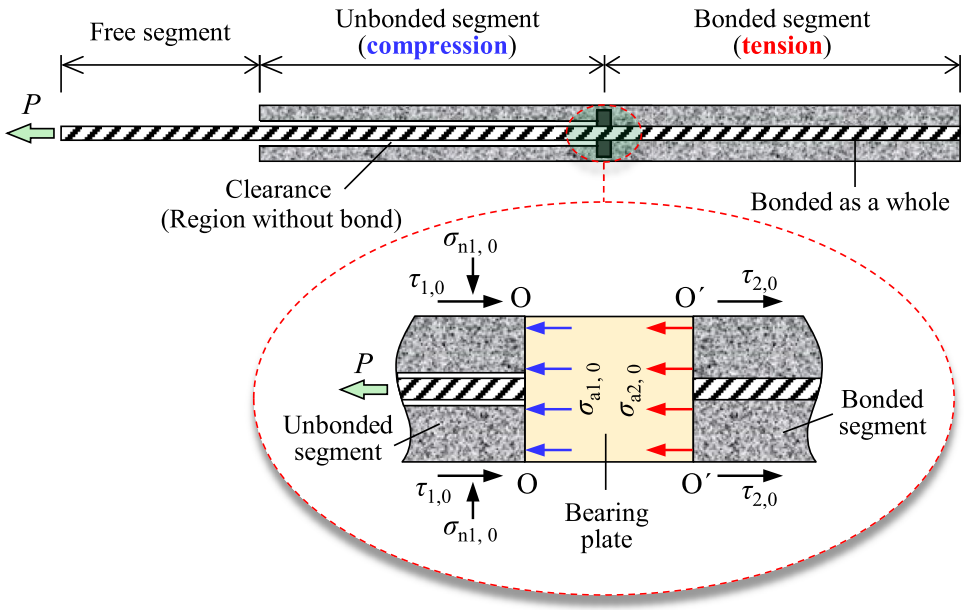

Fig. 8 Stress state of the grout body at bearing plate

two parts, including compressive force P_1 applied to the grout in front of the bearing plate and tensile force P_2 applied to the steel strand behind the bearing plate. In accordance with assumptions (b) and (e), at the junction of the bonded and unbonded segments, that is, the front and rear surfaces of the bearing plate ($x_1 = 0$, $x_2 = 0$), the axial stresses of the grout body should satisfy Eq. (32). Noteworthy that $\sigma_{a1,0}$ and $\sigma_{a2,0}$ are not deliberately distinguished as positive or negative values in Eq. (32). This does not affect the calculation results and is convenient for analysis.

$$P = P_1 + P_2 = \sigma_{a1,0} \cdot A + \sigma_{a2,0} \cdot A \tag{32}$$

where P denotes the pullout load exerted on the anchor head; P_1 and P_2 denote the compressive force and tensile force subjected to the unbonded and bonded segments, respectively; $\sigma_{a1,0}$ is the axial compressive stress of the grout body at the beginning of the unbonded segment; $\sigma_{a2,0}$ is the homogenized axial tensile stress of the integrative entity composed of grout and steel strand at the beginning of the bonded segment; and A is the cross-sectional area of the anchor hole.

4.3 Finite difference solution

The load-transfer governing equations for bonded and unbonded segments (Eqs. 24 and 30) present considerable challenges in terms of achieving the analytical solution. Therefore, the distributions of axial stress, interface shear stress, and displacement over the entire anchorage length will be derived using the finite difference method. The solution methodology can be summarized as follows: The stress distribution over bonded segment is calculated first, and then the stress distribution over unbonded segment is solved through the iterative method with the boundary condition (Eq. 32) serving as the controlling parameter. The detailed steps of the solution process were expounded below.

Step (1): The grout bodies in unbonded and bonded segments are uniformly discretized into n_1 and n_2 units along the axial direction. The lengths of the unbonded and bonded micro-units are L_{au}/n_1 and L_{ab}/n_2, respectively. The generated nodes are numbered along the prescribed local coordinate systems, as shown in Fig. 1. Hereinto, the $n_1 + 1$ nodes in unbonded segment were named $x_{1,0}$, $x_{1,1}$, $x_{1,2}$, …, $x_{1,n1}$, and the $n_2 + 1$ nodes in bonded segment are named $x_{2,0}$, $x_{2,1}$, $x_{2,2}$, …, $x_{2,n2}$ from loaded end to free end in order.

Step (2): The bearing capacity of TCCA is unknown before analysis, so the displacement-controlled method is employed to apply pullout load, with the objective of obtaining precise load–displacement relationship. The free end of bonded segment (node $x_{2,n2}$) is assigned an interface shear displacement of s_a. At the node of $x_{2,n2}$, the axial tensile stress $\sigma_{a2,n2}$ is equal to zero (Eq. 31), and the interface shear stress $\tau_{2,n2}$ can be calculated by Eq. (11).

Step (3): For the node of $x_{2,n2\text{-}1}$ in bonded segment, the axial tensile stress $\sigma_{a2,n2\text{-}1}$ can be calculated by the differential form of Eq. (28), as expressed below.

$$\sigma_{a2,n_2-1} = \frac{u_p \Delta L_{ab}}{A} \tau_{2,n_2} \tag{33}$$

where ΔL_{ab} denotes the length of the analysis bonded micro-units, $\Delta L_{ab} = L_{ab}/n_2$.

The soil–anchor interface shear displacement $s_{2,n2\text{-}1}$ can be calculated by combining Eqs. (26) and (27).

$$s_{2,n_2-1} = s_{2,n_2} + \varepsilon_{a2,n_2-1} \cdot \Delta L_{ab} = s_a + \frac{\sigma_{a2,n_2-1}}{E_{bg}} \Delta L_{ab} \tag{34}$$

where $\varepsilon_{2,n2\text{-}1}$ denotes the axial tensile strain of the anchor body at node $x_{2,n2\text{-}1}$.

The interface shear stress $\tau_{2,n2\text{-}1}$ at node $x_{2,n2\text{-}1}$ can further be determined by substituting $s_{2,n2\text{-}1}$ into Eq. (11).

Step (4): The governing equation for bonded segment (Eq. 29) is rewritten in the difference form, which is employed to calculate the interface shear displacement $s_{2,n2\text{-}2}$.

$$s_{2,n_2-2} = 2s_{2,n_2-1} - s_{2,n_2} + \frac{\mu_p \tau_{2,n_2-1}}{E_{bg} A} \Delta L_{ab}^2 \tag{35}$$

The interface shear stress $\tau_{2,n2\text{-}2}$ at node $x_{2,n2\text{-}2}$ is determined by substituting $s_{2,n2\text{-}2}$ into Eq. (11). The axial tensile stress $\sigma_{a2,n2\text{-}2}$ is calculated by the differential form of Eq. (28), as expressed below.

$$\sigma_{a2,n_2-2} = \sigma_{a2,n_2-1} + \frac{u_p \Delta L_{ab}}{A} \tau_{2,n_2-2} \tag{36}$$

As with node $x_{2,n2\text{-}2}$, the interface shear displacement, interface shear stress, and axial stress for the remaining nodes in bonded segment $x_{2,i}$ (i = 0, 1, …, n_2-3) can be calculated sequentially in the same manner.

Step (5): To facilitate the iterative analysis for unbonded segment, a value of the pullout load P exerted on the anchor head should be assumed. The initial value $P^{(1)}$ is specified as follows for the primary round of iterative calculations.

$$P^{(1)} = 2\sigma_{a2,0} \cdot A \tag{37}$$

where $\sigma_{a2,0}$ denotes the axial tensile stress of the anchor body at the inception of the bonded segment.

In accordance with the boundary conditions (Eq. 32), the axial compressive stress $\sigma_{a1,0}$ of grout body at the loading end of unbonded segment (node $x_{1,0}$) is calculated:

$$\sigma_{a1,0} = \frac{P^{(j)}}{A} - \sigma_{a2,0} \tag{38}$$

where superscript j denotes the number of iterative calculations.

The interface normal stress at node $x_{1,0}$ can be calculated by Eq. (20). As shown in Fig. 8, the interface shear displacements are identical at the front and back surfaces of the bearing plate, that is, $s_{1,0} = s_{2,0}$. Noteworthy that a sudden change in interface shear stress occurs at the junction of bonded and unbonded segments owing to the emergence of normal stress. The interface shear stress $\tau_{1,0}$ can be obtained by substituting $s_{1,0}$ and $\sigma_{n1,0}$ into Eq. (11).

Step (6): Similar to Step (3), the axial compressive stress $\sigma_{a1,1}$ and the interface normal stress $\sigma_{n1,1}$ at node $x_{1,1}$ are calculated using Eqs. (22) and (20) successively. The interface shear displacement $s_{1,1}$ can be determined by combining Eqs. (16) and (21), as shown in Eq. (39). The interface shear stress can then be obtained by Eq. (11).

$$s_{1,1} = s_{1,0} - \varepsilon_{1,1} \cdot \Delta L_{au} = s_{1,0} - \frac{\sigma_{a1,1} - 2v_g \sigma_{n1,1}}{E_g} \Delta L_{au} \tag{39}$$

where ΔL_{au} denotes the length of the analysis unbonded micro-units, $\Delta L_{au} = L_{au}/n_1$; and $\varepsilon_{1,1}$ denotes the axial strain of grout body at node $x_{1,1}$.

Step (7): The load-transfer governing equation for unbonded segment (Eq. 23) is transformed into the differential form at node $x_{1,1}$. The interface shear displacement at node $x_{1,2}$ can further be calculated:

$$s_{1,2} = 2s_{1,1} - s_{1,1} - \frac{u_p \left(2\lambda v_g - 1\right) \tau_{1,1}}{E_g A} \Delta L_{au}^2 \tag{40}$$

The axial compressive stress $\sigma_{a1,2}$, interface normal stress $\sigma_{n1,2}$, and interface shear stress $\tau_{1,2}$ can be determined using Eqs. (22), (20), and (11) successively. Likewise, the remaining nodes in the unbonded segment $x_{1,i}$ (i = 3, 4, …, n_1) are then subjected to a calculation of the stresses and interface shear displacements in sequence.

Step (8): The axial stress at the free end of the unbonded segment is maintained at zero, as this serves as the control condition for the iterative computation. To implement the aforementioned boundary condition (Eq. 31), the range of the pullout load P that is specified in Step (5) is updated:

$$\begin{cases} P_{max}^{(j+1)} = P_{a2,0} + P_{a1,0}^{(j)}, P_{min}^{(j+1)} = P_{min}^{(j)} \text{ if } \sigma_{a1,n_1} > \delta_{err} \\ P_{min}^{(j+1)} = P_{a2,0} + P_{a1,0}^{(j)}, P_{max}^{(j+1)} = P_{max}^{(j)} \text{ if } \sigma_{a1,n_1} < -\delta_{err} \end{cases} \tag{41}$$

where δ_{err} is the prescribed computation accuracy.

The pullout load P is re-valued in a new round of calculations.

$$P^{(j+1)} = \frac{P_{max}^{(j+1)} + P_{min}^{(j+1)}}{2} \tag{42}$$

Steps (5) ∼ (8) are repeated until the prescribed computation accuracy is achieved. Accordingly, the stress distribution over the entire anchorage length can be obtained when the interface shear displacement $s_{2,n2} = s_a$.

Step (9): A new value is assigned to the interface shear displacement at the free end of the bonded segment s_a. Steps (2) through (8) are then repeated to yield the stress distributions for TCCA when subjected to various pullout loads.

Step (10): The pullout load P that meets the computation accuracy has been determined in Step (8). The pullout displacement at the anchor head can be calculated by

Eq. (43). Subsequently, the bearing capacity for TCCA will be ascertained through the generation of pullout load–displacement curve.

$$s_{\mathrm{h}} = s_{1,0} + \Delta_b = s_{1,0} + \frac{P(L_{\mathrm{f}} + L_{\mathrm{au}})}{E_{\mathrm{b}} A_{\mathrm{b}}} \tag{43}$$

where $s_{1,0}$ denotes the interface shear displacement at the free end of the unbonded segment; Δ_{b} represents the tensile deformation of the steel strand or rebar that is not bonded to the grout material.

The axial forces of grout body in both bonded and unbonded segments were not deliberately distinguished as positive or negative values. This does not affect the calculation results and can be convenient for analysis. However, the tensile forces for all grout nodes in bonded segment should be regarded as negative values when presenting the calculation results.

In terms of structural form, TCCA can be viewed as tension anchor, provided that the unbonded length L_{au} is equal to zero. Additionally, TCCA can be considered compression anchor in the absence of bonded segment. Hence, it is reasonable to infer that the developed generalized theoretical framework can also be employed to analyze the load-transfer responses related to both tension anchors and compression anchors. Nevertheless, there are still some limitations of the proposed load-transfer theoretical framework. Especially in some cases, it will no longer be applicable, or the calculation accuracy will deteriorate. For example, (a) the bonded segment is very short, resulting in the separation of the steel strand from the grout during the pullout loading process; (b) the bonded segment disengages from the unbonded segment due to the inadequate adhesion between bearing plate and grout; (c) the interface normal stress σ_{n} is notably large, and the interface shear displacement s_f exhibits considerable variation in response to the interface normal stress σ_{n}, particular for the case of anchors embedded in hard rock. It should be used carefully in the aforementioned instances.

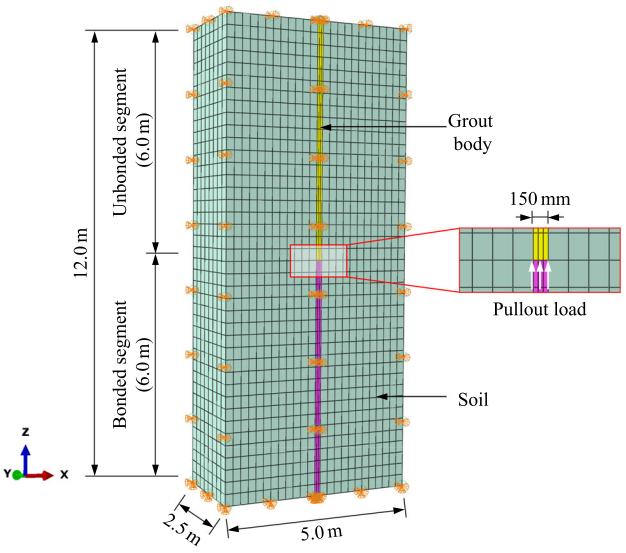

Fig. 9 Panoramic view of the FE model for TCCA

Table 3 Relative errors between FE simulations and theoretical predictions for pullout capacity and ultimate pullout displacement

Type		Tension anchor	Compression anchor	TCCA	
Unbonded length L_{au}: Bonded length L_{ab}		0: 12 m	12 m: 0	6 m: 6 m	
Pullout capacity P_{u}	FEM (kN)	615.7	590.3	694.4	
	Theory (kN)	597.4	603.7	674.1	
	Relative error (%)	3.0	2.3	2.9	
Ultimate pullout displacement $s_{0,\max}$	FEM (mm)	8.9	54.1	30.6	
	Theory (mm)	8.1	55.0	29.0	
	Relative error (%)	9.0	1.7	5.2	

5 FE simulations for verifying the theoretical framework

5.1 FE model design

Three-dimensional finite element (FE) models of tension anchor, compression anchor, and TCCA were developed in ABAQUS. With regard to the theoretical framework verification, the three types of anchors were all 150 mm in diameter of drilling hole, 12 m in whole anchorage length, and 0 m in free length, as shown in Fig. 9. The bonded and unbonded lengths for the three types of anchors are summarized in Table 3. The 3D FE models are 5 m in width, which allows for the elimination of boundary effects. In addition, the anchors exhibit axisymmetric geometrical shape and pullout bearing performance, so the FE models were scaled down to a half-size structure to enhance the computation efficiency. The grout material is cement mortar with Young's modulus of 25 GPa and Poisson's ratio of 0.22. The surrounding soil is 180 MPa in Young's modulus and 0.33 in Poisson's ratio. The steel strand is 32 mm in diameter and 200 GPa in Young's modulus. The soil and the grout body are composed of 8000 linear hexahedral elements (C3D8) and 600 linear wedge elements (C3D6), respectively.

The modeling procedures entailed a series of steps designed to faithfully replicate the bearing characteristics and construction process of TCCAs, including ground stress balance, anchor hole creation, anchor–soil contact, and pullout load application. Each step was executed successively. The program is analogous to those employed for soil nails or tension anchors [38, 42]. The displacement-controlled method was adopted in the loading process of the theoretical modeling. Therefore, this method was also applied in the FE simulations to facilitate the comparison. The pullout load was applied directly at the junction between the bonded and unbonded segments to simplify the FE modeling process, as shown in Fig. 9. The displacement at this junction was designated as the loading control condition for TCCA. The pullout displacements at the beginning and end of the whole anchorage segment were taken as the loading control conditions for tension and compression anchors, respectively. The total pullout displacement at the anchor head is equivalent to the sum of the displacement of the bearing plate and the tensile deformation of the steel strand situated within the unbonded segment.

The non-thickness cohesive elements were employed to simulate the soil–anchor interface mechanical behaviors. The soil–anchor interface damage evolution, as defined in FE models, was specified in exponential form [24, 39]. The interface model parameters were stipulated as: interface elastic shear stiffness $k_c = 7.2 \times 10^4$ kPa.m^{-1}, initiation slip at bond damage $s_c^b = 1.7$ mm, ultimate interface cohesive stress $\tau_c^b = 122.4$ kPa, displacement at complete failure $s_c^u = 35$ mm, and damage evolution rate $\alpha = 1.8$. The developed AFCE interface model was employed to characterize the soil–anchor interface shear behavior within the load-transfer theoretical framework, which differed from the damage model embedded in ABAQUS. It is of paramount importance to guarantee complete concordance between the two study methods with regard to the modeling of interface mechanical behaviors. To achieve this objective, the interface shear stress–displacement curve, which was rendered visible by the exponential damage model, was fitted using Eq. (11), as shown in Fig. 10. Consequently, the AFCE interface model was established with all parameters identified, including τ_{a-} = 120 kPa, $\varphi_\tau = 20°$, $\eta = 0.5$, and $s_f = 2.4$ mm. More details on this strategy can be found in previous publications [43, 44].

5.2 Discussion of the FE simulation results

Figure 11 presents a comparison of pullout load versus displacement responses at the anchor head for TCCA, tension anchor, and compression anchor derived from FE simulations and theoretical predictions. It should be highlighted that the theoretical and simulated curves exhibit excellent matches for all three types of anchors. Table 3 summarizes the relative errors between FE simulations and theoretical predictions of the bearing capacity and the ultimate pullout displacement. Among these three types of anchors, the tension anchor exhibits the greatest discrepancy between predicted and simulated results, with relative errors of 3.0% for ultimate bearing capacity and 9.0% for ultimate pullout displacement. In contrast, the compression anchor exhibits the lowest prediction error. This phenomenon can be explained by the incorporation of interface normal stress into the parameter calibration process for the AFCE interface model. The interface normal stress is zero when analyzing the load-transfer response of tension anchor using the theoretical framework.

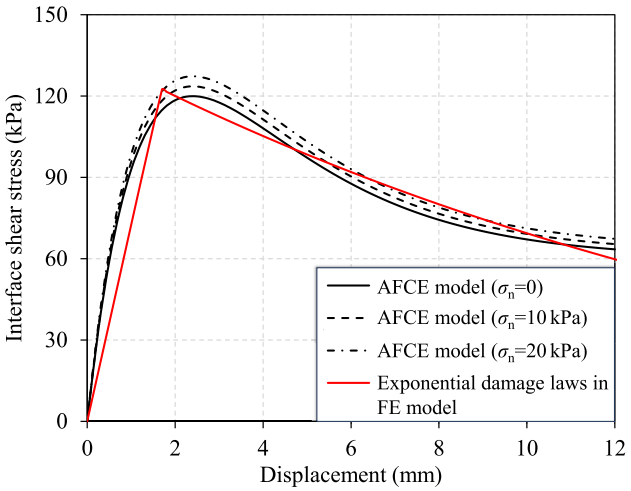

Fig. 10 Comparisons of the characterization for soil–anchor interface behavior between FE simulation and theoretical modeling

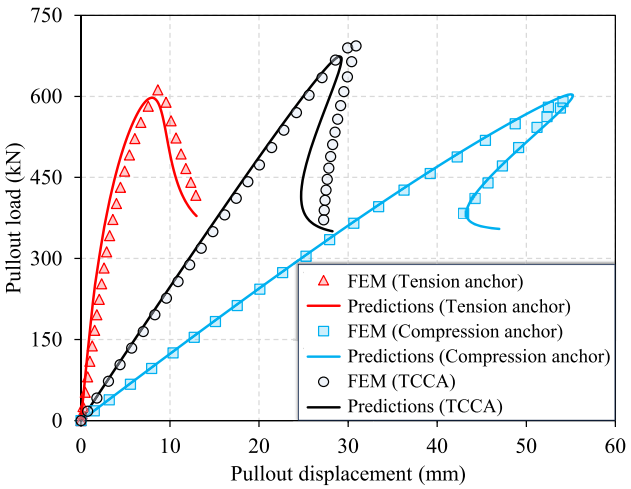

Fig. 11 Comparisons between FEM results and theoretical predictions for *P-s* responses of TCCA, tension anchor, and compression anchor

The TCCA is capable of superior ultimate bearing capacity in comparison with the tension and compression anchors. In this case study, the ultimate bearing capacity of TCCA is 11.4% and 10.4% greater than that of tension anchor and compression anchor when subjected to identical anchorage length. The pullout displacement of compression anchor is the largest among the three types of anchors, primarily due to its longest unbonded length, which allows the steel strand or rebar to stretch freely.

The predicted stress distributions over anchorage segment for tension anchor, compression anchor, and TCCA were compared with the results of FE simulation, as shown in Figs. 12, 13 and 14. The results demonstrate that there is good agreement between theoretical predictions and FE simulations for each type of anchor. Despite some discrepancies in the prediction of interface shear stress distribution when the pullout load is relatively large, the shapes of the predicted and simulated curves still remain comparable. The evidence supports the validity and accuracy of the load-transfer theoretical framework for TCCA.

It can be seen from Figs. 12a and 13a that the axial stress is distributed nonlinearly over anchorage area and transferred in a single direction for tension and compression anchors. Specifically, the axial stress decreases from the head to the end of the anchorage segment for tension anchor, whereas the opposite is true for compression anchor. Another remarkable feature of these two types of anchors is the markedly uneven distribution of interface shear stress (Figs. 12b and 13b), which precludes the mobilization of the soil–anchor interface shear strength to its full potential. Figures 15 and 16 illustrated the evolution processes of axial stress distribution and interface shear stress distribution for TCCA obtained from FE simulation. The axial stress distribution is more linear for TCCA than that observed for tension and compression anchors. Besides, the axial stress is transferred to both the head and end of the anchorage segment for TCCA (Fig. 14a), thereby mitigating the issue of load concentration. An abrupt alteration in axial stress of the grout body is observed at the junction between the bonded and unbonded segments. For example, the maximum axial compressive force and tensile force in unbonded and bonded segments are 323 kN and 327 kN, respectively, when the pullout load P reaches 650 kN. As shown in Figs. 14b and 16, the transfer of interface shear stress occurs in both the front and rear directions. In the case of pullout load with a relatively small magnitude, the peak value of interface shear stress appears at the junction between the bonded and unbonded segments. As the pullout load increases, the peak value of interface shear stress is transmitted gradually to the two ends of the entire anchorage segment. Overall, the distribution of interface shear stress is more uniform for TCCA, which facilitates the simultaneous mobilization of soil–anchor interface shear strength at different positions. This is the rationale behind the greater bearing capacity of TCCA.

6 Performance of the load-transfer theoretical framework in comparison with in-situ and laboratory model experiments

The developed generalized theoretical framework for TCCA can also be utilized for load-transfer analysis associated with both tension anchors and compression anchors. The effectiveness of the theoretical framework is once more evaluated by comparing the predictions with

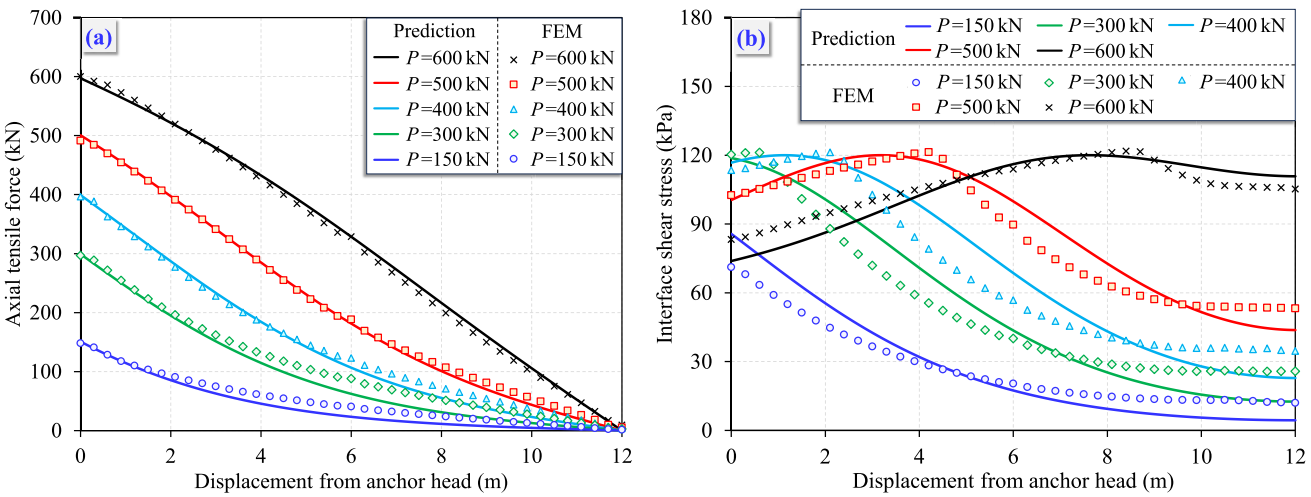

Fig. 12 Comparisons between FEM results and theoretical predictions for stress distributions of tension anchor: **a** Axial tensile force; **b** Interface shear stress

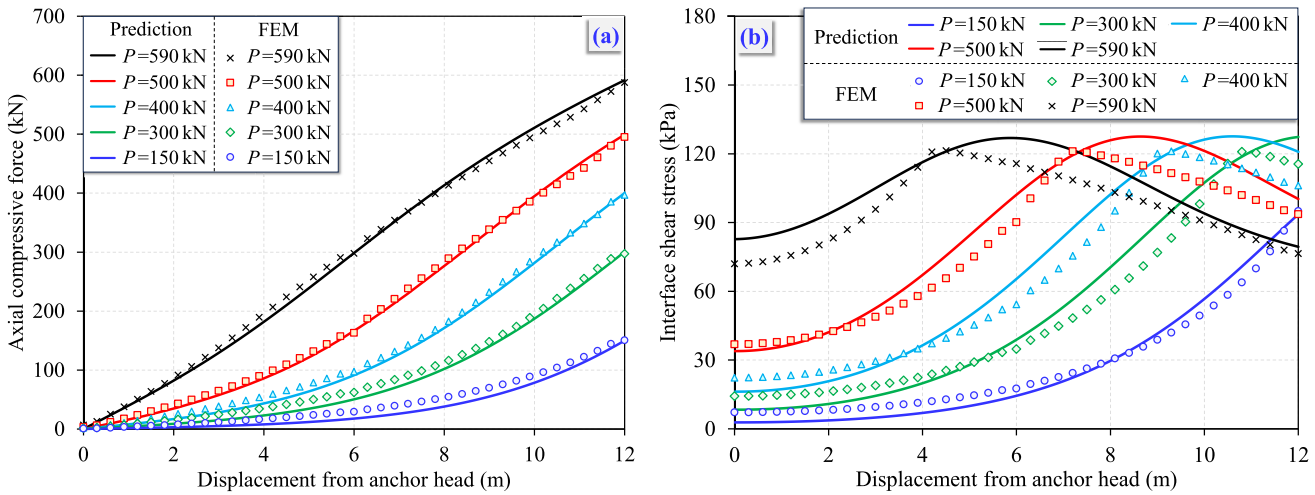

Fig. 13 Comparisons between FEM results and theoretical predictions for stress distributions of compression anchor: **a** Axial compressive force; **b** Interface shear stress

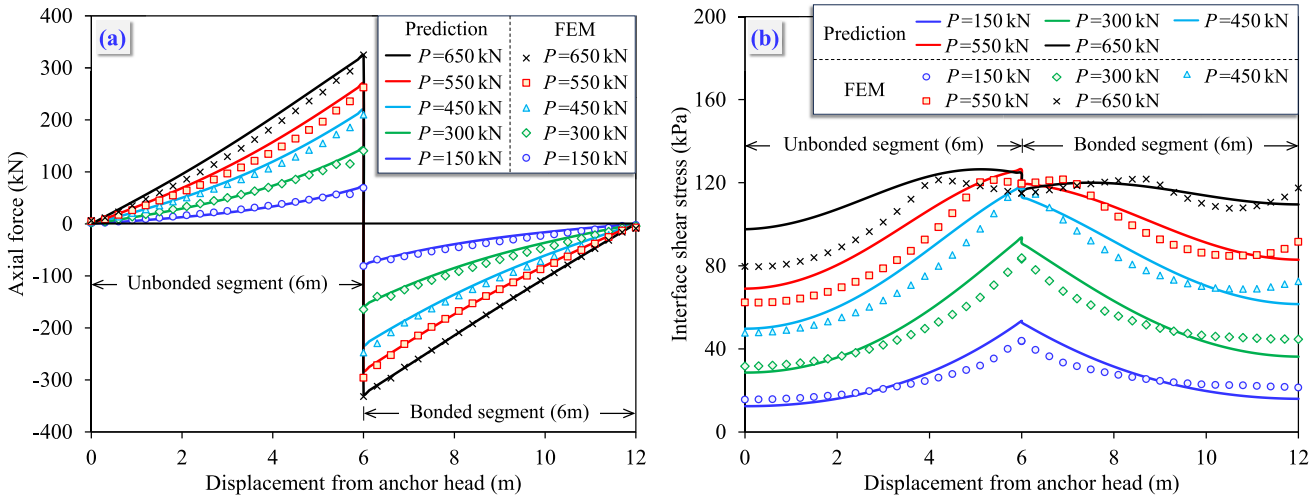

Fig. 14 Comparisons between FEM results and theoretical predictions for stress distributions of TCCA: **a** Axial force; **b** Interface shear stress

those derived from in-situ and laboratory model experiments on the three types of anchors. The following projects with well-documented details are collected and discussed to implement the verification.

6.1 Tension anchors

Rong et al. [25] performed physical model tests to investigate the pullout responses of tension anchors embedded in rock mass. In this test, the reinforcement was hot-rolled steel bar with diameter of 32 mm and Young's modulus of 210 GPa. The rock mass was simulated using concrete with mark of $R_{28}200^{\#}$ (i.e., 28 days curing compressive strength of 200 kg/mm^2), Young's modulus of 25 GPa, and Poisson's ratio of 0.22. The rebar was fully encapsulated in concrete and has a length of 1 m. Strain gauges were plastered on the rebar surface to measure the axial force distribution during loading progress. As a compelling example, the results of this pullout test for tension anchor were also discussed by Chen et al. [4], Ma et al. [18], Martin et al. [20], and Ren et al. [23]. Based on the reported interface characteristic parameters and the original results, the parameters of the AFCE interface model were determined as follows: τ_f = 5450 kPa, η = 0.1, and s_f = 0.16 mm. Figure 17 presents a comparison of pullout load P versus displacement s curve between theoretical prediction and measurements. Figure 18 compares the predicted axial stress distributions under various pullout loads with the corresponding testing data. The predicted P-s curve and the axial stress distributions were both observed to be in good agreement with the measurements, indicating the effectiveness of the proposed theoretical framework for analyzing the load-transfer behaviors of

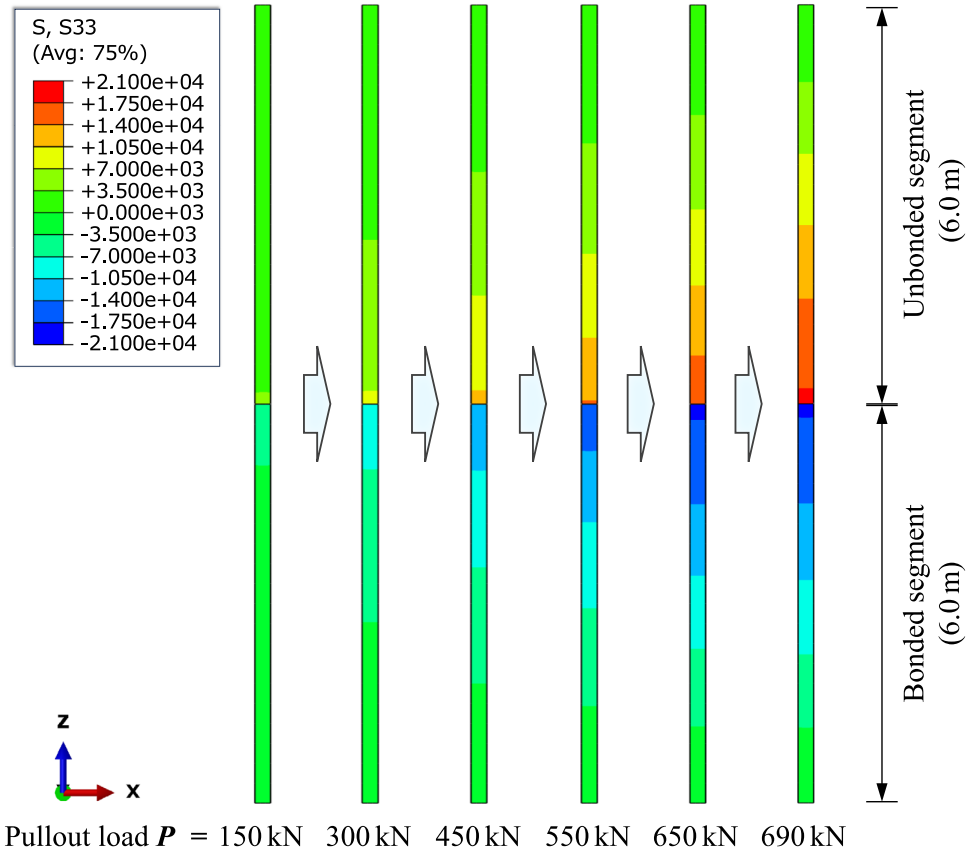

Fig. 15 Evolution of axial stress distribution for TCCA

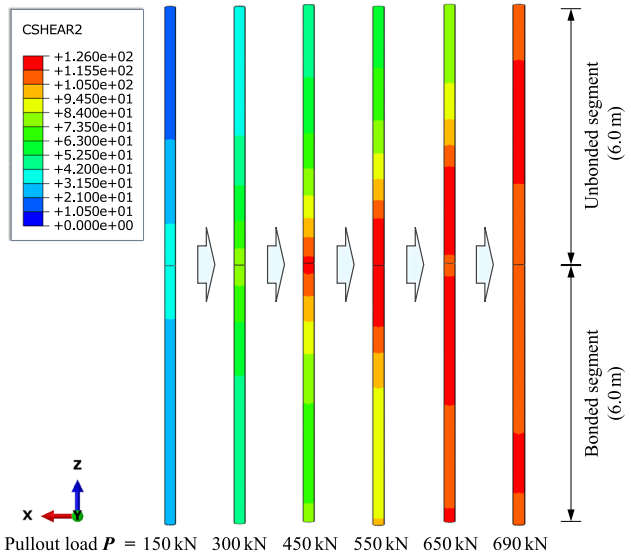

Fig. 16 Evolution of interface shear stress distribution for TCCA

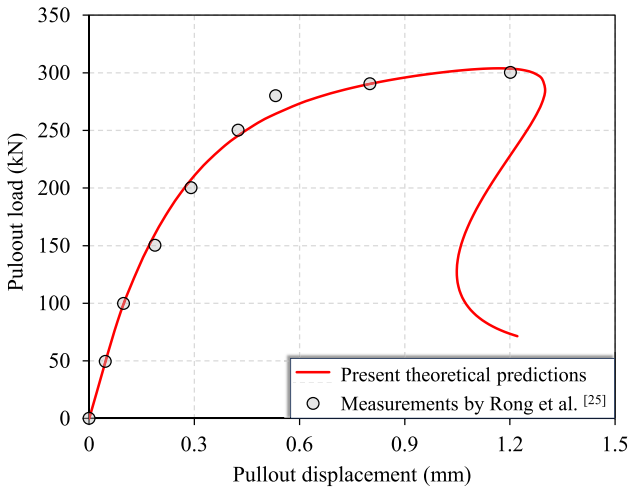

Fig. 17 Comparison of predicted and measured *P-s* curve for tension anchor

tension anchors, as well as the suitability of the model parameters adopted in this case.

6.2 Compression anchors

Ye et al. [37] conducted in–situ pullout tests on recoverable anchors employed in foundation pit engineering. The recoverable anchors belong to compression anchors in regard to their structural connection. The anchors were

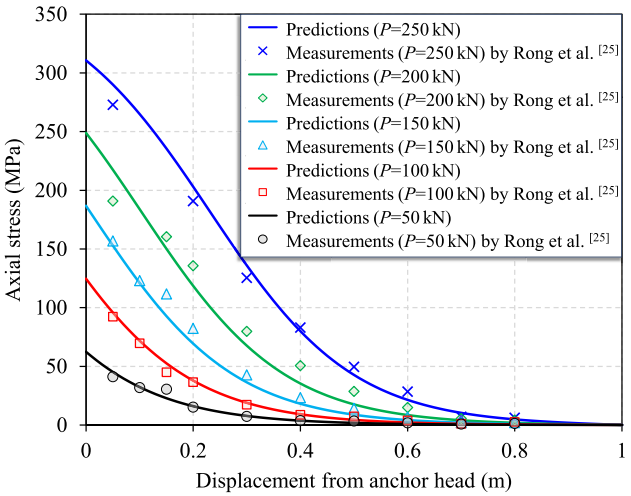

Fig. 18 Comparison of predicted and measured axial stress distribution for tension anchor

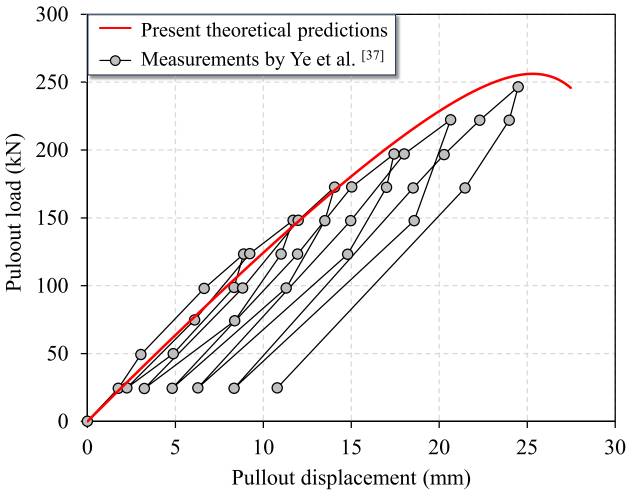

Fig. 19 Comparison of predicted and measured *P-s* curve for compression anchor

7.5 m in anchorage length and 150 mm in diameter of anchor hole. The hot-rolled steel bar used in this test was 28 mm in diameter and 200 GPa in Young's modulus. The cement mortar, serving as the grout material, was cured for 21 days, with Young's modulus of 30 GPa and Poisson's ratio of 0.22. The steel bar is encased in a PVC sleeve to prevent contact with the grout slurry. At the bottom of the anchor hole, the steel bar is connected to the bearing plate. The entire grout body is in compressive stress condition during the loading process. The soil surrounding the anchor is classified as loess, with Young's modulus of 180 MPa and Poisson's ratio of 0.35. It would be preferable to calibrate the interface mechanical model through the implementation of element-scale pullout tests, direct shear tests, or in-situ CPT/SPT. However, it is a significant challenge to find a case that provides results of both in–situ pullout tests for anchors and the corresponding soil–anchor interface shear tests. This difficulty stems from the complexities of simulating the actual construction process and loading conditions of the ground anchors, as well as the physical characteristics of undisturbed soil in an interface shear test. Therefore, the parameters of the AFCE interface model were determined through inversion analysis based on data from the in-situ pullout test and the mechanical characteristics of the soil, including τ_a = 70 kPa, φ_τ = 20°, η = 0.2, and s_f = 8.5 mm. As shown in Fig. 19, the predicted pullout load–displacement curve matches well with the measurements. It indicated that the theoretical load-transfer framework is also suitable for compression anchors and that the parameters are reasonable.

The geometry size is comparable to that of the anchors in actual engineering. Hence, this engineering case was further discussed. The bearing capacity of compression anchor obtained through theoretical calculation is 256.1 kN, and the ultimate pullout displacement is 25.3 mm. In the event that tension anchor and TCCA of the same dimensions are employed in this case, the bearing capacities are predicted to be 247.1 kN and 257.1 kN. Concurrently, the ultimate pullout displacements are 9.6 mm and 16.4 mm. The three types of anchors possess nearly equivalent bearing capacities. This phenomenon can be attributed to two factors: the relatively short anchoring length and the low soil–grout interface shear strength. The parametric studies conducted in Sect. 7 also corroborated this point with greater specificity. However, the pullout displacement of compression anchor is the largest because its freely stretchable rebar is the longest. In this engineering case, the anchor structure type can be freely selected according to the construction or design requirements, if no consideration is given to the pullout displacement.

6.3 TCCAs

Tu et al. [30] carried out the in-situ pullout tests for TCCAs. The anchor was 3.0 m in anchorage length, 1.0 m in free length, and 150 mm in diameter of anchor hole. The grout material was cement paste with water–cement ratio of 0.5 and Young's modulus of 30 GPa. The reinforcement used in this test was hot-rolled steel bar with diameter of 22 mm and Young's modulus of 200 GPa. The anchor was entirely embedded in sandy clay. Young's modulus and Poisson's ratio for the surrounding sandy clay were 120 MPa and 0.33, respectively. The test result of TC21 was discussed in this paper. In the current test, the length ratio between bonded and unbonded segments was 2:1. In other words, the bonded length L_{ab} is 2.0 m, while the unbonded length L_{au} is 1.0 m. The bearing plate situated at the junction between the bonded and unbonded segments is

made of steel, with diameter of 90 mm and thickness of 20 mm. In unbonded segment, PVC sleeve was wrapped around the steel bar to prevent contact with the grout. Based on inversion analysis for the in-situ pullout test data and the mechanical characteristics of the soil, the parameters of the AFCE interface model were determined as follows: τ_a = 42 kPa, φ_τ = 24°, η = 0.5, and s_f = 28 mm. It can be observed from Fig. 20 that again the agreement of *P-s* curve for TCCA between the theoretical prediction and the in-situ measurement is excellent.

Tu et al. [33] also conducted the laboratory pullout model tests for TCCA. The model test results for the group of TC360-12 were collected to verify the load-transfer theoretical framework. There are four parallel specimens in this group of tests. The length ratio of bonded and unbonded segments was 1:2. Hereinto, the anchor was 120 mm in bonded length L_{ab}, 240 mm in unbonded length L_{au}, and 50 mm in diameter of anchor hole. The grout material was cement paste with water–cement ratio of 0.5 and Young's modulus of 30 GPa. The reinforcement used in this test was screw rod with diameter of 18 mm and Young's modulus of 200 GPa. The concrete with a mark of C30 was used to simulate the rock around the anchor. The pullout load is implemented by displacement-controlled method at a rate of 0.01 mm/s. Based on the statistical results by Tu et al. [33] and inversion analysis for the test data, the parameters of the AFCE interface model were determined as follows: τ_a = 1500 kPa, φ_τ = 20°, η = 0.55, and s_f = 2.8 mm. Figure 21 compares the pullout load–displacement response obtained from theoretical analysis and model tests. It can be seen that the predictions and the measurements are matched well again.

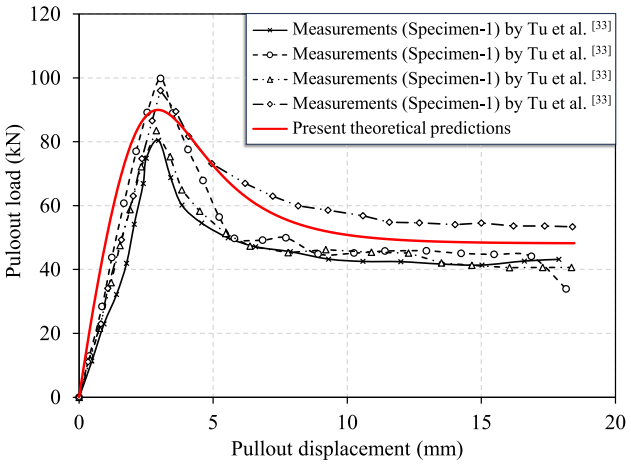

Fig. 21 Comparison of predicted and measured *P-s* curve for TCCA (test data from Tu et al. [33])

7 Parametric studies

In the developed theoretical load-transfer framework, the bearing performance of TCCA is dependent on some parameters, such as geometry size of the anchor, mechanical properties of the grout material and the surrounding soil, and the soil–anchor interface shear properties. A series of parametric studies were carried out to investigate the effect of some key parameters on the bearing capacity of TCCA. The scopes of some geometric and material parameters in the following discussion are representative of TCCAs that are usually used in engineering applications. The parameters of the AFCE interface model were selected on the basis of the values derived from Sub-Sect. 5.1.

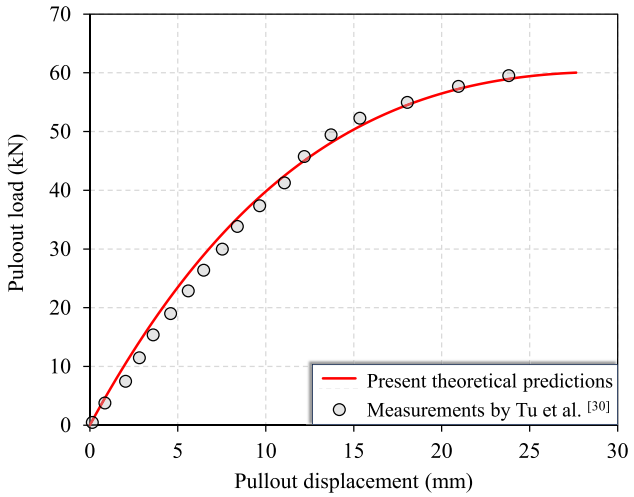

Fig. 20 Comparison of predicted and measured *P-s* curve for TCCA (test data from Tu et al. [30])

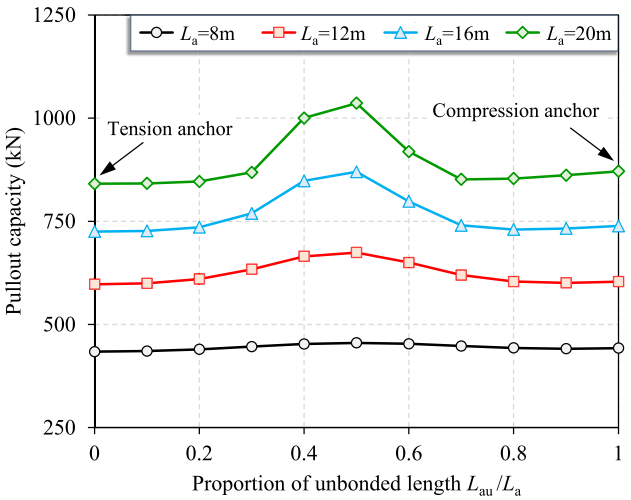

Fig. 22 Variation in the pullout capacity with the proportion of unbonded length

7.1 Effect of proportion of unbonded length

Figure 22 depicts the variation in the pullout capacity with the proportion of unbonded length L_{au}/L_a for TCCAs with different anchorage lengths. The bearing capacity of TCCAs initially exhibits an increase, followed by a subsequent decline as increasing the value of L_{au}/L_a. When $L_{au}/L_a = 0.5$ (i.e., the bonded length is equal to the unbonded length), the TCCAs achieve the maximum bearing capacity. The influence of the proportion of unbonded length on the bearing capacity is more pronounced in the case of TCCAs with longer anchorage lengths. In the present discussion, the influence exerted by the proportion of unbonded length can almost be ignored when anchorage length $L_a = 8$ m.

7.2 Effect of anchorage length

The variations in bearing capacity of tension anchor, compression anchor, and TCCA with anchorage length were assessed, as shown in Fig. 23. Hereinto, the proportion of unbonded length for TCCA was specified as 0.5. It can be seen that the bearing capacities for the anchors increase with the increase in anchorage length, but the rates decrease gradually. Among these three types of anchors, TCCA is equipped with the largest bearing capacity, while the tension anchor exhibits the minimum. When the anchorage length is less than 10 m, the three types of anchors exhibit a nearly identical bearing capacity, which indicates that the structural form of the anchor exerts a negligible influence on performance. When the anchorage length exceeds 10 m, TCCA exerts a greater bearing capacity than the tension anchor and compression anchor. The difference is found to intensify as the anchorage length increases. As a result, TCCA will be recommended in situations where the anchors need a longer length to achieve sufficient bearing capacity. Otherwise, the configuration of anchor structure can be selected flexibly according to the deformation and construction demands.

7.3 Effect of residual strength ratio

The residual strength ratio η serves as an indicator of the magnitude of soil–anchor interface softening. A smaller value of η signifies a more significant interface softening characteristic. Figure 24 plots the pullout force versus displacement curves for tension anchor, compression anchor, and TCCA with varying residual strength ratios. The pullout displacement is the least for tension anchor due to the absence of an unbonded segment and the shortest steel strand or rebar that can be stretched freely. Conversely, compression anchor is distinguished by the longest unbonded segment and the longest free steel strand or rebar, so it exhibits the largest pullout displacement. In addition, in the event that the soil–anchor interface residual strength ratio is relatively small, the pullout force at the anchor head will experience a notable reduction following the attainment of the ultimate pullout load. It demonstrates that the brittle failure characteristics of the anchors are more pronounced.

The variations in the pullout capacity with anchorage length for tension anchors and TCCAs with different interface residual strength ratios are illustrated in Fig. 25. It can be observed that the interface residual strength ratio exerts negligible influence on the bearing capacity of tension anchors and TCCAs in cases where their anchorage lengths are less than 10 m and 20 m, respectively. However, a reduction in the interface residual strength ratio

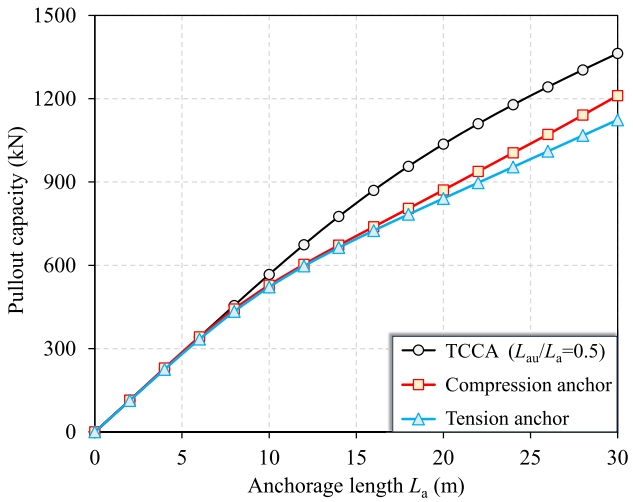

Fig. 23 Variation in the pullout capacity with anchorage length for tension anchor, compression anchor, and TCCA

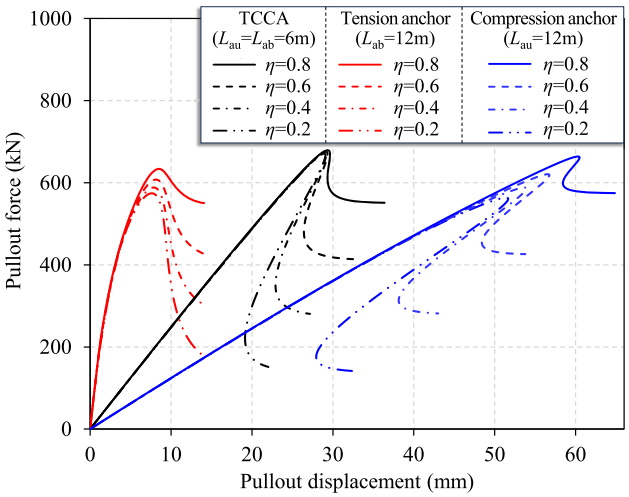

Fig. 24 Pullout responses for the three types of anchors with different interface residual strength ratios

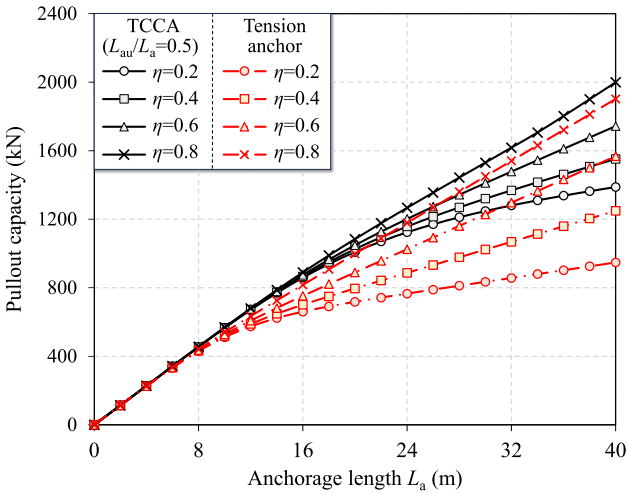

Fig. 25 Variation in the pullout capacity with anchorage length for tension anchors and TCCAs with different interface residual strength ratios

results in a corresponding reduction in the anchor's bearing capacity, accompanied by an increasing discrepancy in bearing capacity between TCCA and tension anchor, particularly when the anchorage length is large. Noteworthy that there will be merely a slight improvement in the anchor's bearing capacity provided that the anchorage length exceeds a certain threshold and continues to increase. This observation underscores the necessity and importance of considering the effective anchorage length. In the current discussion, when η is equal to 0.2, the effective anchorage lengths are 12 m and 24 m for the tension anchor and TCCA, respectively. The effective anchorage length of TCCA is longer than that of the tension anchor and compression anchor and is approximately twice that of the latter. The utilization of TCCAs represents an intelligent choice in instances where the soil–anchor interface shows evident softening characteristics and a long anchorage length is required to satisfy the bearing requirements.

8 Summary

A novel AFCE interface model was developed in this study, the parameters of which can be identified through the utilization of several interface shear characteristic values. Based on the AFCE interface model, a generalized load-transfer theoretical framework for TCCA was proposed using finite difference method. Three-dimensional FE simulations were conducted on the bearing performance of tension anchor, compression anchor, and TCCA to verify the load-transfer theoretical framework. The predicted stress distributions and load–displacement responses were compared with the results obtained from FE simulations, in-situ tests, and laboratory model tests. Comparative analyses were performed to assess the consistency between the predicted stress distributions and load–displacement responses and the results from FE simulations, as well as in-situ and laboratory model tests. Parametric studies were finally conducted.

9 Conclusions

The primary findings derived from the present investigation are as follows:

(1) The proposed AFCE interface shear model comprises only three parameters, yet is capable of characterizing both the interface softening and hardening behaviors, and the effect of interface normal stress can also be considered. The effectiveness of this model was verified through the close matches between the predicted interface shear stress–shear displacement curves and the measurements obtained from element-scale pullout tests and interface direct shear tests.

(2) The theoretically calculated pullout load–displacement responses and stress distributions for tension anchors, compression anchors, and TCCAs all show satisfactory agreement with the results derived from FE simulations, in-situ, and laboratory model tests. It provides evidence that the developed generalized load-transfer theoretical framework is suitable for analyzing the pullout responses of all three types of anchors.

(3) The distribution of interface shear stress is more uniform for TCCAs in comparison with tension and compression anchors. This uniformity reflects the simultaneous mobilization of interface shear strength in both bonded and unbonded segments as well as the mitigation of load concentration problem, so TCCAs are equipped with greater bearing capacity.

(4) The bearing capacity of TCCAs initially exhibits an increase followed by a subsequent decline as the proportion of unbonded length increases. When the proportion of unbonded length is equal to 0.5 (i.e., the bonded length is equal to the unbonded length), the TCCAs achieve the maximum bearing capacity.

(5) TCCAs will be recommended in situations where the soil–anchor interface exhibits evident softening characteristics and a long anchorage length is necessary to satisfy the bearing requirements. Otherwise, the configuration of anchor structure can be flexibly chosen according to the deformation and construction demands.

Table 4 Calculation results of bonded segment (s_a = 1.0 mm)

Calculation sequence	Node	Distance from anchor head (m)	$P_{a2}(x_2)$ (kN)	$s_2(x_2)$ (mm)	$\tau_2(x_2)$ (kPa)
1	$x_{2,100}$	12	0.00	1.0000	92.89
2	$x_{2,99}$	11.94	− 2.63	1.0003	92.90
3	$x_{2,98}$	11.88	− 5.25	1.0008	92.93
4	$x_{2,97}$	11.82	− 7.88	1.0016	92.97
…	…	…	…	…	…
98	$x_{2,3}$	6.18	− 291.25	2.3949	120.00
99	$x_{2,2}$	6.12	− 294.64	2.4253	119.99
100	$x_{2,1}$	6.06	− 298.03	2.4560	119.98
101	$x_{2,0}$	6	− 301.42	2.4870	119.94

Table 5 Calculation results of axial compressive force $P_{a1}(x_1)$ in unbonded segment (s_a = 1.0 mm)

Calculation sequence	Node	Distance from anchor head (m)	Axial compressive force $P_{a1}(x_1)$ at different number of iterations (kN)				
			1	2	…	17	18
1	$x_{1,0}$	6	150.712	226.069	…	288.300	288.302
2	$x_{1,1}$	5.94	147.217	222.521	…	284.710	284.711
3	$x_{1,2}$	5.88	143.724	218.975	…	281.121	281.122
4	$x_{1,3}$	5.82	140.232	215.431	…	277.534	277.535
…	…	…	…	…	…	…	…
98	$x_{1,97}$	0.18	− 176.166	− 91.756	…	6.597	6.599
99	$x_{1,98}$	0.12	− 179.419	− 94.931	…	4.395	4.398
100	$x_{1,99}$	0.06	− 182.667	− 98.111	…	2.196	2.199
101	$x_{1,100}$	0	− 185.911	− 101.294	…	-0.001	0.001

Table 6 Calculation results of interface normal stress $\sigma_{n1}(x_1)$ in unbonded segment (s_a = 1.0 mm)

Calculation sequence	Node	Distance from anchor head (m)	Interface normal stress $\sigma_{n1}(x_1)$ at different number of iterations (kPa)				
			1	2	…	17	18
1	$x_{1,0}$	6	10.115	15.172	…	19.348	19.349
2	$x_{1,1}$	5.94	9.880	14.934	…	19.108	19.108
3	$x_{1,2}$	5.88	9.646	14.696	…	18.867	18.867
4	$x_{1,3}$	5.82	9.411	14.458	…	18.626	18.626
…	…	…	…	…	…	…	…
98	$x_{1,97}$	0.18	− 11.823	− 6.158	…	0.443	0.443
99	$x_{1,98}$	0.12	− 12.041	− 6.371	…	0.295	0.295
100	$x_{1,99}$	0.06	− 12.259	− 6.584	…	0.147	0.148
101	$x_{1,100}$	0	− 12.477	− 6.798	…	0.000	0.000

Table 7 Calculation results of interface shear displacement $s_1(x_1)$ in unbonded segment (s_a = 1.0 mm)

Calculation sequence	Node	Distance from anchor head (m)	Interface shear displacement $s_1(x_1)$ at different number of iterations (mm)				
			1	2	…	17	18
1	$x_{1,0}$	6	2.487	2.487	…	2.487	2.487
2	$x_{1,1}$	5.94	2.467	2.457	…	2.448	2.448
3	$x_{1,2}$	5.88	2.448	2.427	…	2.410	2.410
4	$x_{1,3}$	5.82	2.428	2.398	…	2.373	2.373
…	…	…	…	…	…	…	…
98	$x_{1,97}$	0.18	2.700	1.677	…	0.741	0.741
99	$x_{1,98}$	0.12	2.725	1.690	…	0.740	0.740
100	$x_{1,99}$	0.06	2.750	1.703	…	0.740	0.740
101	$x_{1,100}$	0	2.775	1.717	…	0.740	0.740

Table 8 Calculation results of interface shear stress $\tau_1(x_1)$ in unbonded segment (s_a = 1.0 mm)

Calculation sequence	Node	Distance from anchor head (m)	Interface shear stress $\tau_1(x_1)$ at different number of iterations (kPa)				
			1	2	…	17	18
1	$x_{1,0}$	6	123.621	125.461	…	126.980	126.980
2	$x_{1,1}$	5.94	123.560	125.409	…	126.936	126.936
3	$x_{1,2}$	5.88	123.493	125.343	…	126.867	126.867
4	$x_{1,3}$	5.82	123.419	125.263	…	126.773	126.774
…	…	…	…	…	…	…	…
98	$x_{1,97}$	0.18	115.065	112.307	…	77.855	77.854
99	$x_{1,98}$	0.12	114.886	112.452	…	77.780	77.778
100	$x_{1,99}$	0.06	114.699	112.597	…	77.724	77.723
101	$x_{1,100}$	0	114.504	112.743	…	77.690	77.688

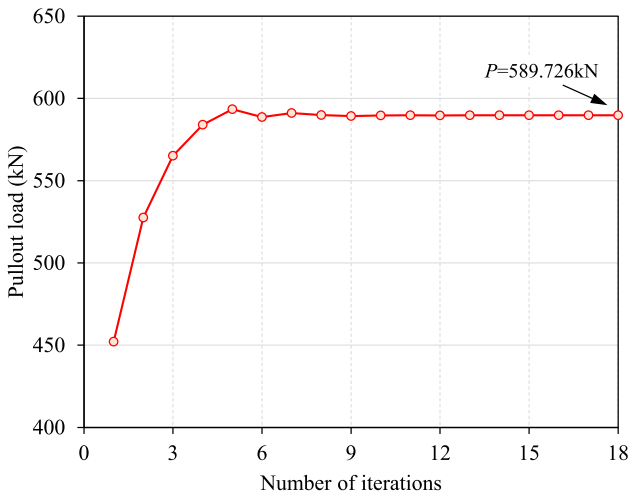

Fig. 26 The convergence process of pullout load at anchor head during iterative calculation (s_a = 1.0 mm)

Appendix: A calculation example of the finite difference solution

The anchor geometry size and the parameters of the AFCE interface model were selected on the basis of the values derived from Sub-Sect. 5.1. As the calculation example, the interface shear displacement at the free end of bonded segment (node $x_{2,n2}$) s_a was assigned to be 1.0 mm. Besides, the numbers of grout units $n_1 = n_2 = 100$, computation accuracy $\delta_{err} = 0.001$. The axial force $P_{a2}(x_2)$, interface shear displacement $s_2(x_2)$, and interface shear stress $\tau_2(x_2)$ of the bonded segment can be directly calculated, as shown in Table 4. The unbonded segment was then analyzed by iterative calculation. Tables 5, 6, 7 and 8 summarize the calculation results of axial force $P_{a1}(x_1)$, interface normal stress $\sigma_{n1}(x_1)$, interface shear displacement $s_1(x_1)$, and interface shear stress $\tau_1(x_1)$ of the bonded segment, respectively. Figure 26 illustrates the convergence process of the pullout load at anchor head during iterative calculation.

Acknowledgements This research was sponsored by the Shandong Provincial Natural Science Foundation (No. ZR2024QE444), the National Natural Science Foundation of China (No. 52278349), the Hunan Provincial Key Laboratory for Big Data Smart Application of Natural Disaster Risks Survey of Highway Engineering (No. BNH2024KFA03), and the Higher Education Scientific Research Project 2024 (No. 24SY0104). The authors appreciate their financial support.

Funding Natural Science Foundation of Shandong Province, ZR2024QE444, Shimin Zhu, National Natural Science Foundation of China, 52278349, Changfu Chen, Hunan Provincial Key Laboratory for Big Data Smart Application of Natural Disaster Risks Survey of Highway Engineering, BNH2024KFA03, Shimin Zhu, Higher Education Scientific Research Project, 24SY0104, Mingbin Wang.

Data availability All data, models, and code generated or used during the study appear in the submitted article.

Declarations

Conflict of interest The authors declare no competing interests.

References

1. Briaud JL, William FP, Weatherby DE (1998) Should grouted anchors have short tendon bond length? J Geotech Geoenviron Eng 124(2):110–119. https://doi.org/10.1061/(ASCE)1090-0241(1999)125:9(808)
2. Cai Y, Esaki T, Jiang YJ (2004) An analytical model to predict axial load in grouted rock bolt for soft rock tunnelling. Tunn Undergr Space Technol 19:607–618. https://doi.org/10.1016/j.tust.2004.02.129
3. Chen CF, Zhu SM (2024) Element-scale pullout test study on the mechanical behavior of grouted anchor–soil interface subjected to ground pressure. Acta Geotech 19:5433–5447. https://doi.org/10.1007/s11440-024-02256-5
4. Chen CF, Zhu SM, Zhang GB, Morsy AM, Zornberg JG, Mao FS (2022) A generalized load-transfer modelling framework for tensioned anchors integrating adhesion-friction-based interface model. Int J Geomech 22(5):04022036. https://doi.org/10.1061/(ASCE)GM.1943-5622.0002338
5. Chen WB, Hong CY, Chen XS, Luo GB, Su D (2023) Comparative analysis of anchor cables in pullout tests using distributed fiber optic sensors. Can Geotech J 60:1861–1876. https://doi.org/10.1139/cgj-2022-0455
6. Chu LM, Yin JH (2005) Comparison of interface shear strength of soil nails measured by both direct shear box tests and pullout tests. J Geotech Geoenviron Eng 131:1097–1107. https://doi.org/10.1061/(ASCE)1090-0241(2005)131:9(1097)
7. Ehrlich M, Silva RC (2015) Behavior of a 31m high excavation supported by anchoring and nailing in residual soil of gneiss. Eng Geol 191:48–60. https://doi.org/10.1016/j.enggeo.2015.01.028
8. Farmer IW (1975) Stress distribution along a resin grouted rock anchor. Int J Rock Mech Min Sci Geomech Abstr 12:347–351. https://doi.org/10.1016/0148-9062(75)90168-0
9. Hajiabdolmajid V, Kaiser PK, Martin CD (2003) Mobilised strength components in brittle failure of rock. Géotechnique 53(3):327–336. https://doi.org/10.1680/geot.2003.53.3.327
10. Hong CY, Yin JH, Zhou WH, Pei HF (2012) Analytical study on progressive pullout behavior of a soil nail. J Geotech Geoenviron Eng 138(4):500–507. https://doi.org/10.1061/(ASCE)GT.1943-5606.0000610
11. Hu LM, Pu JL (2004) Testing and modeling of soil-structure interface. J Geotech Geoenviron Eng 130:851–860. https://doi.org/10.1061/(ASCE)1090-0241(2004)130:8(851)
12. Kim NK (2003) Performance of tension and compression anchors in weathered soil. J Geotech Geoenviron Eng 129(12):1138–1150. https://doi.org/10.1061/(ASCE)1090-0241(2003)129:12(1138)
13. Kim NK, Park JS, Kim SK (2007) Numerical simulation of ground anchors. Comput Geotech 34:498–507. https://doi.org/10.1016/j.compgeo.2006.09.002
14. Kong C, Yang T, Xiao M, Yuan QT (2023) Numerical simulation of fully grouted rock bolts with or without faceplates based on the tri-linear bond-slip model. Constr Build Mater 367:130288. https://doi.org/10.1016/j.conbuildmat.2022.130288
15. Kou HL, Guo W, Zhang MY (2015) Pullout performance of GFRP anti-floating anchor in weathered soil. Tunn Undergr Space Technol 49:408–416. https://doi.org/10.1016/j.tust.2015.06.001
16. Lee SW, Kim TS, Sim BK, Kim JS, Lee IM (2012) Effect of pressurized grouting on pullout resistance and group efficiency of compression ground anchor. Can Geotech J 49:939–953. https://doi.org/10.1139/t2012-059
17. Li C, Stillborg B (1999) Analytical models for rock bolts. Int J Rock Mech Min Sci 36(8):1013–1029. https://doi.org/10.1016/S1365-1609(99)00064-7
18. Ma SQ, Nemcik J, Aziz N (2013) An analytical model of fully grouted rock bolts subjected to tensile load. Constr Build Mater 49:519–526. https://doi.org/10.1016/j.conbuildmat.2013.08.084
19. Maleki J, Pak A, Yousefi M, Aghakhani N (2022) A comprehensive FE study for design of anchored wall systems for deep excavations. Tunn Undergr Space Technol 122:104340. https://doi.org/10.1016/j.tust.2021.104340
20. Martín LB, Tijani M, Hadj-Hassen F (2011) A new analytical solution to the mechanical behaviour of fully grouted rockbolts subjected to pull-out tests. Constr Build Mater 25(2):749–755. https://doi.org/10.1016/j.conbuildmat.2010.07.011
21. Pang YS, Liu HL, Gong JY (2010) Study of pullout tests of recoverable anchors. Rock Soil Mech 31(6):1813–1826+1821. https://doi.org/10.16285/j.rsm.2010.06.009
22. Pham TA, Nadimi S, Sutman M (2024) Softening-based interface model and nonlinear load-settlement response analysis of piles in saturated and unsaturated multi-layered soils. Comput Geotech 171:106331. https://doi.org/10.1016/j.compgeo.2024.106331
23. Ren FF, Yang ZJ, Chen JF, Chen WW (2010) An analytical analysis of the full-range behaviour of grouted rockbolts based on a tri-linear bond-slip model. Constr Build Mater 24:361–370. https://doi.org/10.1016/j.conbuildmat.2009.08.021
24. Rezazadeh M, Carvelli V, Veljkovic A (2017) Modeling bond of GFRP rebar and concrete. Constr Build Mater 153:102–116. https://doi.org/10.1016/j.conbuildmat.2017.07.092
25. Rong G, Zhu HC, Zhou CB (2004) Testing study on working mechanism of fully grouted bolts of thread steel and smooth steel. Chin J Rock Mech Eng 23(3):469–475
26. Shin GB, Jo BH, Kim SR, Chung CK, Baek SH (2023) Field study on behavior of load distributive compression anchor installed in weathered rock and soft rock. Can Geotech J 60:1895–1908. https://doi.org/10.1139/cgj-2022-0384
27. Sun HL, Lu W, Zhao D, Li DB (2024) Analytical method for interfacial slip failure processes based on UFL bond-slip model: study of grout/soil anchorage interfaces in earthen sites. Comput Geotech 176:106778. https://doi.org/10.1016/j.compgeo.2024.106778
28. Sun JP, Dong PT, Yu TT (2024) Assessing stability of 3D slopes reinforced with prestressed anchor cables considering strength reserve. Comput Geotech 174:106596. https://doi.org/10.1016/j.compgeo.2024.106596

29. Toufigh V, Shirkhorshidi SM, Hosseinali M (2017) Experimental investigation and constitutive modeling of polymer concrete and sand interface. Int J Geomech 17(1):04016043. https://doi.org/10.1061/(ASCE)GM.1943-5622.0000695
30. Tu BX, Cai YY, He JF, Yu J, Xu GP, Cheng Q (2019) Analysis of anchorage performance on new tension-compression anchor III field test. Chin J Geotech Eng 41(5):846–854. https://doi.org/10.11779/CJGE201905007
31. Tu BX, Liu C, Zhang LH, Wang HT (2022) Influence of grout's poisson effect on interfacial shear stress for compression anchor in rock mass. Geotech Geol Eng 40:857–869. https://doi.org/10.1007/s10706-021-01931-8
32. Tu BX, Liu SY, Yu J, He JF, Zhou JF, Jia JQ (2018) Analysis of anchorage performance on new tension-compression anchor: I simplified theory. Chin J Geotech Eng 40(12):2289–2295. https://doi.org/10.11779/CJGE201812017
33. Tu BX, Yu J, He JF, Cheng Q, Xu GP, Jia JQ (2019) Analysis of anchorage performance on new tension-compression anchor II: model test. Chin J Geotech Eng 41(3):475–483. https://doi.org/10.11779/CJGE201903009
34. Wong KS, The CI (1995) Negative skin friction on piles in layered deposits. J Geotech Eng 121(6):457–465. https://doi.org/10.1061/(ASCE)0733-9410(1995)121:6(457)
35. Wu XZ, Wang G, Jiang YJ, Gong B, Li B (2015) Mechanism of CTC-yield bolts and its experimental research. Chin J Geotech Eng 37(1):139–147. https://doi.org/10.11779/CJGE201501017
36. Yang WD, Wang XP, Ivanović A, Zhang X (2023) Coupled analytical solutions for circular tunnels considering rock creep effects and time-dependent anchoring forces in prestressed bolts. Tunn Undergr Space Technol 134:104954. https://doi.org/10.1016/j.tust.2022.104954
37. Ye SH, Zhao ZF, Wu Q, Pan LM (2020) Study on the anchorage performance of recoverable steel anchors in loess stratum in northwest China. Chin J Ground Improv 2(3):196–202. https://doi.org/10.3785/j.issn.2096-7195.2020.03.004
38. Ye XY, Wang SY, Wang Q, Sloan SW, Sheng DC (2017) Numerical and experimental studies of the mechanical behaviour for compaction grouted soil nails in sandy soil. Comput Geotech 90:202–214. https://doi.org/10.1016/j.compgeo.2017.06.011
39. Yu SS, Zhu WC, Niu LL, Zhou SC, Kang PH (2019) Experimental and numerical analysis of fully grouted long rockbolt load-transfer behavior. Tunn Undergr Space Technol 85:56–66. https://doi.org/10.1016/j.tust.2018.12.001
40. Zhang GB, Chen CF, Zornberg JG, Morsy AM, Mao FS (2020) Interface creep behavior of grouted anchors in clayey soils: effect of soil moisture condition. Acta Geotech 15:2159–2177. https://doi.org/10.1007/s11440-019-00907-6
41. Zhang QQ, Zhang ZM (2012) A simplified nonlinear approach for single pile settlement analysis. Can Geotech J 49:1256–1266. https://doi.org/10.1139/t11-110
42. Zhou WH, Yin JH, Hong CY (2011) Finite element modeling of pullout testing on a soil nail in a pullout box under different overburden and grouting pressures. Can Geotech J 48:557–567. https://doi.org/10.1139/T10-086
43. Zhu SM, Chen CF, Mao FS, Cai H (2021) Application of disturbed state concept for load-transfer modeling of recoverable anchors in layer soils. Comput Geotech 137:104292. https://doi.org/10.1016/j.compgeo.2021.104292
44. Zhu SM, Chen CF, Zhang GB, Wang MB, Zhang ZW (2024) A theoretical model for the load-transfer analyses of load distributive compression anchor integrating DSC-based interface nonlinear model. Constr Build Mater 449:138250. https://doi.org/10.1016/j.conbuildmat.2024.138250
45. Zou JF, Zhang PH (2019) Analytical model of fully grouted bolts in pull-out tests and in situ rock masses. Int J Rock Mech Min Sci 113:278–294. https://doi.org/10.1016/j.ijrmms.2018.11.015